Revision #1 (7/30/2014)

Trinitite redux: Mineralogy and petrology

G. Nelson Eby[1*], Norman Charnley[2], Duncan Pirrie[3], Robert Hermes[4], John Smoliga[5] and Gavyn Rollinson[6]

[1]Department of Environmental, Earth & Atmospheric Sciences, University of Massachusetts, Lowell, MA 01854, U.S.A.

[2]Department of Earth Sciences, University of Oxford, South Parks Road, Oxford OX1 3AN, U.K.

[3]Helford Geoscience LLP, Trelowarren Mill Barn, Mawgan, Helston, Cornwall, TR12 6AE, U.K.

[4]Los Alamos, New Mexico, U.S.A.

[5]Roxbury, Connecticut, U.S.A.

[6]Camborne School of Mines, University of Exeter, CEMPS, Penryn Campus, Penryn, Cornwall, TR10 9FE, U.K.

[*]E-mail: nelson_eby@uml.edu

ABSTRACT

Trinitite is the glass formed during the first atomic bomb test near Socorro, New Mexico, on July 16, 1945. The protolith for the glass is arkosic sand. The majority of the glass is bottle green in color, but a red variety is found in the northern quadrant of the test site. Glass beads and dumbbells, similar in morphology to micro-tektites, are also found at the Trinity site. The original description of this material, which appeared in American Mineralogist in 1948, noted the presence of two glasses with distinctly different indices of refraction (n = 1.46 and 1.51-1.54). Scanning electron microscopy (SEM) and **Q**uantitative **E**valuation of **M**inerals by **SCAN**ning

electron microscopy (QEMSCAN®) analysis is used to investigate the chemical composition and fine-scale structure of the glass. The glass is heterogeneous at the 10s of micron scale with discrete layers of glass showing flow-like structures. The low index of refraction glass is essentially SiO_2 (high-Si glass), but the higher index of refraction glass (low-Si glass) shows a range of chemical compositions. Embedded in the glass are partially melted quartz (α-quartz as determined by X-ray diffraction) and feldspar grains. The red trinitite consists of the same two glass components along with additional Cu-rich, Fe-rich and Pb-rich silicate glasses. Metallic globules are common in the red trinitite.

In terms of viscosity, the high-Si and low-Si glasses differ by several orders of magnitude, and there is minimal mixing between the two glasses. QEMSCAN® analysis reveals that there are a number of chemical subgroups (which can be characterized as simple mixtures of melted mineral components) within the low-Si glasses, and there is limited mixing between these glass subgroups. The red trinitite contains regions of Fe-rich glass which show sharp contact with surrounding Fe-poor glass. Both the textural and chemical data suggest that these two glasses existed as immiscible liquids. The metallic droplets in the red trinitite, which consist of variable amounts of Cu, Pb and Fe, show textural evidence of unmixing. These metals are largely derived from anthropogenic sources – Cu wire, Pb bricks, and the steel tower and bomb casing. The combination of mineralogical and chemical data indicate that temperatures on the order of 1600 ^{o}C and pressures of at least 8 GPa were reached during the atomic detonation and that there was a reducing environment during cooling, as evidenced by the presence of native metals, metal sulfides, and a low Fe^{3+}/Fe^{2+} ratio. Independent estimates of maximum temperature during the detonation are on the order of 8000 K, far higher than suggested by the mineral data. This discrepancy is probably due to the very short duration of the event. In all respects, the trinitite

glasses are similar to tektites and fulgurites, and by analogy one conclusion is that temperature estimates based on mineralogical observations for these materials also underestimate the maximum temperatures.

Keywords: Trinitite, fused arkose, glass melting, heterogeneous glasses, liquid immiscibility, melt viscosity, QEMSCAN®

INTRODUCTION

The Atomic Age started on July 16, 1945, at 5:29 am Mountain War Time in a remote patch of desert near Socorro, New Mexico. The defining event was the detonation of the first nuclear device, a plutonium fission bomb (the "gadget"). During the nuclear detonation the arkosic sand surrounding the blast site was fused forming a green glassy material now referred to as trinitite. The origin of the name is somewhat obscure. The earliest known use of the term "trinitite" was in a letter dated October 22, 1945, from Louis Hempelmann, who was in charge of the Los Alamos Health Physics group. Before that the material was variously referred to in official correspondence as Trinity dirt, crust and slag, glass, fused glass and TR glass (William Kolb, 2013, personal communication). Trinitite was first described in the scientific literature by Ross (1948) in American Mineralogist. In March 1952, the AEC [Atomic Energy Commission] announced it was letting a contract to have the trinitite at GZ (Ground Zero) cleaned up. Much of the remaining trinitite was eventually graded up and buried while the crater was smoothed over with a shallow mix of sand and trinitite shards. The work was completed in July 1953 (Jim Eckles, 2013, personal communication). Although the Trinity site is now occasionally opened to visitors, collecting is prohibited. Samples are available from commercial suppliers, from amateur mineral collectors and from scientists at Los Alamos National Laboratory.

Since the original report by Ross (1948) most trinitite studies have been concerned with the radiological aspects of the material (Parekh et al. 2006; Fahey et al. 2010). More recently, because of the realities of current world affairs, trinitite studies have focused on the forensic aspects of a nuclear detonation (Eby et al. 2010a; Fahey et al. 2010; Belloni et al. 2011; Bellucci and Simonetti 2012; Bellucci et al. 2013). Trinitite also shares many characteristics with fulgurites (fused glasses produced by lightning strikes) and tektites (fused glasses produced by meteorite impacts) that are also formed by high temperature short duration events. The purpose of this study is to characterize trinitite in terms of its mineralogy and petrology using modern X-ray analysis techniques.

PREVIOUS STUDIES AND CHARACTERIZATION OF TRINITITE

In his initial study of the Trinity glasses, Ross (1948) reported that the glass was pale bottle green in color, extremely vesicular, and in places contained embedded grains of quartz and feldspar. The parent material was arkosic sand consisting of "angular quartz grains, abundant feldspar including both microcline and smaller amounts of plagioclase, together with small amounts of calcite, hornblende, and augite in a matrix of sandy clay" (Ross 1948, p. 360). Ross (1948) recognized that there were two types of glass. One had a refractive index of n = 1.51 to 1.54 while the other had a refractive index of n = 1.46. He concluded that the higher index glass was formed from the feldspars, clay materials, and accessory minerals in the arkosic sand while the lower index glass was essentially pure silica. Ross (1948) also made the important observation that the higher index glass appeared to have been much more fluid than the lower index glass, i.e. the viscosity of the fused quartz glass (lower index) was such that it did not flow while the fused feldspar-clay mixture had a lower viscosity and did flow. Ross (1948) also noted that in one small area in the northern quadrant of the blast site there was glass that was oxblood

red in color. He attributed the color to the presence of copper and today this particular glass is referred to as red trinitite.

Staritzky (1950) reported the results of a 1949 field study of the Trinity site. At that time the glass cover had not been removed. He noted that the central area, within a 30 meter radius of the tower foundation, did not have a continuous glass cover. Within this area Staritzky found 2 to 5 mm diameter glass beads, the first reported occurrence, and ascribed their origin to melt droplets that had been suspended in the blast cloud. From 30 to 210 meters from the tower foundation the glass cover was continuous and the crust thickness was on the order of 1 to 2 cm. From 210 to 340 meters from the tower foundation the glass formed "a discontinuous lacy pattern, eventually grading into vermicular bodies and scattered pellets of sand held together by minor amounts of glass" (Staritzky 1950, p. 3). Based on site measurements of the thickness and areal extent of the glass, petrographic observations, and some simplified calculations Staritzky (1950) estimated that 1.7×10^6 kg of glass had been formed at a temperature of greater than 1470 ^{o}C and that the amount of energy used to fuse the glass was $4.3 \pm 0.5 \times 10^{12}$ joules.

Glass et al. (1987) related the beads (and dumbbell shaped glass also found at Trinity) to tektites. Infrared analysis of water content in trinitite glass fragments and beads varied between 0.01 and 0.05 wt. % water. Furthermore, the magnetic intensity for trinitite glass beads was close to zero as is the case for tektites. The $Fe^{3+}/Fe^{2+} = \sim 0.1$ is also similar to tektites. Based on their observations of the shape and size of the trinitite glass beads and dumbbells, and the measured physical and chemical properties, Glass et al. (1987) concluded that they were similar in virtually all respects to tektites.

It is now recognized that there are a number of varieties of trinitite at the the Trinity site (Eby et al. 2010b):

(1) Glassy trinitite consists of fragments and splatter of bottle green glass (Fig. 1a).

(2) Pancake trinitite consists of a 1 to 5 cm thick layer of green glass (Fig. 1b) that formed on top of the arkosic sand. The underside of the glass layer has numerous embedded mineral grains.

(3) Red trinitite (Fig. 1c) found to the north of ground zero. The red color is due to the presence of copper. Aerial photographs of the Trinity site show several power lines running to the site from the north and it is the copper in these wires that presumably is the source of the copper in the red trinitite. Red trinitite also contains metallic spherical inclusions consisting of Fe, Cu, and Pb (Eby et al. 2010b, Fig. 5). The Pb was derived from Pb bricks that were used at the test site and the Fe is most likely from the tower, bomb casing, and supports for the transmission lines.

(4) Bead and dumbbell shaped trinitite (Fig. 2), very similar to tektites, is widely distributed at the site. This material has been referred to as "anthill trinitite" because it is collected by ants when they construct their anthill and is found around the top of the anthill (Eby et al. 2010b, Fig. 9).

SAMPLES AND ANALYTICAL PROCEDURES

The trinitite glass fragments, beads and dumbbells, investigated in this study were collected at the Trinity site by Robert Hermes, Los Alamos National Laboratory. The samples were collected from anthills both within and outside the inner perimeter fence.

X-ray diffraction data were collected using a Bruker AXS X-Ray Powder Diffractometer Model D8 Advance, CuKα radiation (1.54Å) in Bragg-Brentano parafocusing mode, with a graphite monochromator and a scintillation detector. Samples were ground to a powder and

packed into a zero background silicon holder. Step scans were obtained at 40 kV, 40 mA, using a scan range of 2° - 50° (2)θ, and a counting time of 10 seconds per step.

Scanning Electron Microscopy (SEM) data were obtained at the University of Oxford, Department of Earth Sciences, using a JEOL JSM-840A SEM with Oxford Instruments Isis 300 ED (Energy Dispersive) system and intrinsic Ge detector. For spot mode on an image the beam is of the order of 0.25 μm diameter and the excitation volume is 2 to 5 μm (depending on the material). For broad beam analysis of glasses or other sensitive materials a raster is used over a 5 x 4 μm area. Routine analytical conditions are 20 kV accelerating voltage and 6 nA beam current. Standards are pure oxides and elements and well characterized silicate standards. Corrections are made using the ZAF procedure. For oxide amounts greater than 0.5 wt% estimated precision and accuracy are better than 5% relative.

Four uncovered polished epoxy mounts were analyzed using automated scanning electron microscopy with linked energy dispersive analyzers using the QEMSCAN® 4300(**Q**uantitative **E**valuation of **M**inerals by **SCANn**ing electron microscopy) at the Camborne School of Mines, University of Exeter, UK. QEMSCAN® technology was originally developed for the mining industry, but has been widely used in the geosciences (e.g. Pirrie and Rollinson 2011; Potter et al. 2011; Armitage et al. 2013). The system used in this study is based on a Zeiss Evo 50 SEM with four light element Bruker Xflash® Silicon Drift energy dispersive (ED) X-ray detectors controlled by iMeasure v. 4.2 software for data acquisition and iDiscover v. 4.2 software for spectral interpretation and data processing. The QEMSCAN® was set up to run at an accelerating voltage of 25 kV and a beam current of 5 nA.

The QEMSCAN® system identifies the location of particles within the area of a thin section using a predefined backscatter electron threshold which separates the mounting media

from the sample. In the Fieldscan measurement mode, the particles are then systematically mapped at an operator defined beam stepping interval, in this case 5 μm. At each analysis point an ED spectrum is acquired and automatically assigned to a mineralogical or chemical compositional grouping (see Pirrie et al. 2004, 2009, for discussions of QEMSCAN® measurement modes). The acquisition of each ED spectrum is achieved in about 10 milliseconds, hence the sample can be mapped at very high resolution. During data processing, pixels with closely similar chemical or mineralogical groupings are combined. The resulting output consists of high resolution compositional maps of the particles analyzed and the modal mineralogy/phase compositions.

RESULTS

XRD analysis

The arkosic sand at the Trinity site consists of angular grains of quartz, K-feldspar, plagioclase, muscovite, calcite, pyroxene, amphibole, and sparse rock fragments (Ross 1948, Eby et al. 2010b). X-ray diffraction data (Fig. 3) were obtained for the arkosic sand and trinitite glass fragments and beads. Quartz, muscovite, albite, microcline, and actinolite were identified in the arkosic sand. The only crystalline phase identified in the various trinitite glasses was alpha quartz, the low temperature and low pressure quartz polymorph.

SEM and QEMSCAN® results

Conventional SEM and QEMSCAN® techniques have been used to characterize the various trinitite glasses. Some of the conventional SEM results were previously reported in Eby et al. (2010b). Here we present the complete data set for the trinitite glasses and the newly acquired QEMSCAN® results. Two red trinitite fragments and 15 green trinitite fragments, distributed across 4 mounts, were analyzed by QEMSCAN®. Two of the mounts (A and B)

consist of single red trinitite specimens. Mount C has three green glass fragments and Mount D has twelve green glass fragments. All the QEMSCAN® images are found in electronic Appendix I. Supplemental Images. The complete set of results for the spot SEM analyses is found in electronic Appendix II. Supplemental Data Table.

The QEMSCAN® data is organized into the following compositional groups: quartz, K-feldspar, Ca Al silicate, Al Ca K silicate, Ca Al Fe silicate, Ca Al K silicate, Fe Ca Al silicate, Ca silicates and metal phases which include Cu metal, Cu silicates and Fe oxides. For the two mineral groups, the chemical composition approximates that of the named mineral but the scanned areas may be, and often are, glass. Quartz occurs as partially resorbed grains that are still optically identifiable (and produce X-ray diffraction patterns). Feldspar occurs as angular fragments, but many of the areas mapped as K-feldspar are glasses. The other chemically-determined groupings do not correspond to a particular mineral composition and all these areas are glass or, in the case of the metals, discrete metallic droplets (see Fig. 5, Eby et al. 2010b).

Modal abundances for the various chemical groups, derived from the QEMSCAN® images, are reported in Table 1. Note that these modal abundances are for the entire mount. Thus in the case of Mount C (3 fragments) and Mount D (12 fragments) these are average values for all the green trinitite glass fragments in the mount.

Green trinitite

Green trinitite (BD3). Conventional SEM back scattered electron (BSE) and QEMSCAN® images for BD3 are shown in Fig. 4. In combination the two images provide a wealth of information. On the left hand side of the images (areas labeled Kfs and Qtz) a remnant K-feldspar and a quartz grain are in contact. The irregular boundary between the two suggests that melting was occurring along this contact. The pink areas on the QEMSCAN® image (the

dark areas on the SEM image) are melted quartz grains that still retain their chemical identity. The brightest areas on the SEM image are Ca Al silicate glass which forms a long stringer. The stringer is surrounded by Ca Al K silicate glass which marks the transition to the abundant Al Ca K silicate glass. Also note the diffuse green areas on the QEMSCAN® image that have the composition of K-feldspar and represent digested feldspar grains. These same areas can be distinguished on the SEM image by a difference in gray tone. The bulk of the material in the glass falls in the Al K Ca silicate group and represents a relatively homogeneous glass phase. While the QEMSCAN® image (Fig. 4b) is very useful for distinguishing chemically discrete areas of the glass, the SEM image (Fig. 4a) more clearly shows the flow features. SEM spot analyses for the different components are reported in Table 2.

Green trinitite (BD8). The contact between the arkosic sand and trinitite glass is shown at the top of the images (Fig. 5). The quartz grains in the sand are fractured and angular compared to the "quartz" areas seen in the glass. The K-feldspar grains in the arkosic sand have been partially melted as demonstrated by the embayments in the grains and the diffuse outlines of some of the grains. The residual K-feldspar grains in the glass are diffuse and have been completely melted and largely incorporated into the glass. The glass infilling between the quartz and K-feldspar grains in the arkosic sand consists of Ca Al Fe silicate, Al Ca K silicate and Ca Al K silicate glasses. Discrete chemical domains are found within the glass and the areas identified as quartz are largely glass. A distinctive Ca Al silicate glass band extends across the top part of the image and there are other smaller Ca Al silicate glass bands. There are also discrete bands of Al Ca K silicate and Ca Al K silicate glass. The images reveal the extreme heterogeneity of the glass. The SEM spot analyses are reported in Table 3. Compared to BD3,

BD8 is richer in CaO (excluding the Ca Al silicate components), 6.7 ± 2.2 versus 9.8 ± 2.8 wt% and poorer in Al_2O_3, 14.8 ± 1.4 versus 12.5 ± 1.4 wt%.

Green trinitite (BD11). The bulk of this sample compositionally approximates a mixture of Ca Al silicate glass and Ca Al K silicate glass (Fig. 6). Embedded in the glass are small blobs of "quartz" glass. A large K-feldspar grain occurs along the left side of the glass fragment and the grain is rimmed sequentially by Al Ca K silicate glass and then Ca Al K silicate glass towards the glass matrix. The SEM image (Fig. 6a) clearly shows bands of Ca Al silicate glass in the Ca Al K silicate glass. As with the previous examples this grain shows compositional variations at the 10 to 100 μm level as evidenced by discrete bands with different compositions.

Red trinitite

Red Trinitite (RTS). BSE and QEMSCAN® images for this red trinitite fragment (Mount A, Sample RTS) are shown in Figure 7. The round bright areas on Figure 7a are metallic droplets (a close-up view and elemental maps for one of these droplets can be found in Eby et al. 2010b, Fig. 5). The QEMSCAN® image (Fig. 7b) clearly shows the remnant and partially melted quartz (pink) and K-feldspar (green) grains. Note the rounded edges and embayments in many of these grains. The dark gray areas in Figure 7c are the remnant quartz grains and most of the smaller grains are now glass but have still retained their physical integrity (i.e. they did not mix with the surrounding liquid, now glass). The dark gray fractured grains in Figure 7d are remnant K-feldspars.

SEM spot analyses were made on several of the phases in the red trinitite (RTS, Fig. 7c, 7d, Table 4). SiO_2 varies from 49.6 to 68.3 wt% and is the major component of the glasses. Copper is found in all analyses. As is well known from ceramics, reduced copper oxide gives an oxblood red color (Daniel 2013), the same color shown by red trinitite. The bright areas in Fig.

253 7d are characterized by high concentrations of Pb (reported as PbO). Iron occurs in the several
254 wt% range and is probably largely of anthropogenic origin, as is the copper (from the
255 transmission lines) and lead (from lead bricks that were scattered in the immediate area).

256 For the red trinitite (RTS, Mount A, Fig. 7) the major compositional groups are (in vol%)
257 quartz (31.6%), Al Ca K silicate (23.7%), Ca Al silicates (17.4%), and K-feldspar (6.1%). The
258 metal phases comprise 4.6% of the sample.

259 **Red Trinitite (RTL).** BSE and QEMSCAN® images for this red trinitite fragment
260 (Mount B, Sample RTL) are shown in Figure 8. Remnant quartz and feldspar grains are
261 dispersed in a glassy matrix. Many of the grains show corroded margins. The major
262 compositional groups (in vol%) are quartz (26.4%), Al Ca K silicate (19.6%), Ca Al silicate
263 (14.6%), Ca Al Fe silicate (9.8%), K-feldspar (8.0%), and Fe Ca Al silicate (5.5%). The metal
264 phase comprises 2.72% of the sample. Of note is that the compositional groups that contain
265 significant Fe comprise a much greater proportion of this sample compared to RTS. The olive
266 green areas on the QEMSCAN® image are Fe-rich silica glasses (Table 4, analyses RTL2, RTL3,
267 RTL4, and RTL8). As was the case for RTS, all of the silicate glasses contain Cu.

268 Areas of Fe-rich silica glass are shown in Figure 8c and 8d. On Figure 8c the dark areas
269 are remnant quartz grains (spot 1). The bright area (spots 2, 3, and 4) is Fe-rich silica glass. The
270 change in brightness is due to a change in the concentration of Pb (greater for spot 4 relative to
271 spots 2 and 3). Note the curvilinear contact between the Fe-rich glass and the silicate glass. On
272 Figure 8d, spot 7 is a remnant melted quartz grain, spot 8 is Fe-rich silica glass and spot 9 is
273 silicate glass.

274 **Metallic inclusions.** A variety of metallic inclusions are found in red trinitite (Fig. 9).
275 The source of the metals are iron from the bomb casing and support structures, lead from lead

bricks scattered in the immediate vicinity of ground zero, and copper from the transmission lines that ran north from ground zero. A significant miscibility gap exists at high temperatures in the Cu-Fe-Pb system and this gap increases with decreasing temperature (Burton 1991; Onderka et al. 2013; Wang et al. 2005). During cooling Cu-rich, Fe-rich, and Pb-rich liquids form because of this miscibility gap.

Inclusion I1 (Fig. 9a) contains several large Fe-blebs in a Cu-Pb matrix. The brighter areas in the matrix are Pb-rich and presumably formed during cooling which led to an increase in the Cu-Pb miscibility gap. Note that in the Cu-Pb matrix there are several small angular Fe regions which are probably unmelted Fe fragments.

Inclusion I2 (Fig. 9b) is a small rounded Fe particle with arcuate blebs of copper along the outer edge. Small bright spots in the Fe are Cu-rich. The shape of the interface between the Cu and Fe is typical of that formed between two immiscible liquids indicating that copper has the higher surface tension (Belkin and Horton 2009).

Inclusion I3 (Fig. 9c) is a mixture of Cu and Fe with Fe-rich blebs and dendrites. These features are indicative of rapid cooling. In the matrix the lighter areas are richer in Cu compared to the darker areas (which are richer in Fe). Of note is that the separation of Fe and Cu is not complete in this sample, i.e. the liquid was quenched before significant phase separation could occur.

In inclusion I4 (Fig. 9d) a Fe-rich bleb occurs in an irregular shaped Cu-Fe matrix. This is the most complex metallic inclusion observed in our specimens. The bright spots in the Fe-bleb are Pb. Also note what appear to be exsolution lamellae in the Fe-bleb. In the Cu-Fe matrix the brighter regions are Cu-rich. The Fe-rich area in the upper right of the image is interpreted as a

298 partially melted iron fragment. Given its shape, the Fe-bleb must have existed as a separate
299 liquid droplet that became embedded in a partially molten Fe-Cu fragment.

300 ## DISCUSSION

301 In the initial description of trinitite Ross (1948) distinguished two types of glass based on
302 their refractive indices. The lower index glass was almost pure silica while the higher index glass
303 was inferred to consist of a mixture of feldspars and ferromagnesian silicates with much lower
304 silica content. The QEMSCAN results similarly fall into two groups, one largely composed of
305 silica (melted quartz grains) while the other has much lower silica contents. However, at the 10s
306 to 100s of micron scale this lower silica glass shows a great deal of variability ranging from
307 some layers that are very calcium rich to others that are richer in alkalis and alumina. In addition,
308 silicate glasses with high lead content and high iron content are found in the red trinitite. Also of
309 note is the presence of quench textures in some of the metallic globules which points to the rapid
310 cooling of the liquids. Therefore we are dealing with a disequilibrium situation in which liquids
311 of different chemical compositions quickly solidified without significant interaction thus forming
312 layering at the 10s of microns scale.

313 ### Physical conditions of the trinitite melting experiment

314 Initial descriptions of the site referred to the trinitite layer as a fused glass layer (Staritzky
315 1950). Hermes and Strickfaden (2005) argued that the trinitite surface layer was deposited as a
316 trinitite "rain" derived from melted material from the blast crater. They estimate that the fireball
317 duration for the Trinity event was 3.1 seconds and the total time with a "hot cloud" was 14-20
318 seconds. Based on films and photographs of the blast, Semkow et al. (2006) estimate a "freeze
319 out time" (the time when the glass solidified) of 8-11 seconds. The trinitite "rain" rate was 0.36
320 cm s^{-1} which would lead to a glass layer ~1 cm thick (actual observed thicknesses vary between

1 and 2 cm). Contact between the trinitite glass and the underlying arkosic sand is seen in Fig. 5. Note that the feldspar and quartz grains are partially melted and that the trinitite glass (which was liquid at the time of formation) has infiltrated the pore spaces between the arkosic sand grains, an observation which supports the trinitite "rain" model. Also found at the site are glass beads and dumbbells, distributed over a wide area and found up to 1.8 km from ground zero.

Hermes and Strickfaden (2005) estimated that the average fireball temperature was 8430 K. This is well above the temperature required to melt all the mineral components in the arkosic sand. Partially and completely melted (high- Siglass) quartz grains are common. At atmospheric pressure quartz melts at ~1720 ^{o}C (Deer, Howie, and Zussman 1992). We have also observed 10 to 20 μm zircon grains that are apparently unmelted. Zircon begins to melt at ~1680^{o}C (Butterman and Foster 1967). According to the QEMSCAN® results (Appendix II. Supplemental Data Table) RTS, RTL, and green trinitite in Mount C contain 0.002, 0.003, and 0.003 vol%, respectively, zircon. Zircon was not identified in Mount D. Large K-feldspar grains are occasionally found as inclusions in trinitite and these have partially melted (as illustrated in Fig. 6, also note the areas of disaggregated K-feldspar shown in Fig. 4). There are two factors which play a role in the melting of the arkosic sand – temperature and the duration of high temperatures. While very high temperatures were achieved, the duration of these high temperatures was short, thus some of the higher melting temperature minerals were not completely fused.

Only α-quartz has been identified in X-ray diffraction studies of trinitite glass fragments and beads (Fig. 3). Optical examination of trinitite in thin section reveals partially melted quartz grains (Fig. 10a). Also noted in some of the quartz grains are what appear to be Planar Deformation Features (PDFs, Fig. 10b). PDFs, compared to Planar fractures (Pfs), occur as

multiple sets of narrow (<2-3 μm), closely spaced (typically 2-10 μm) straight planes (French 1998). The formation of PDFs in quartz requires pressures of at least 8 GPa (Gratz et al. 1996, Koeberl 1997). At this pressure coesite is the stable SiO_2 polymorph. However, if coesite did form it must have inverted to α-quartz as the pressure fell. Presumably this inversion would be facilitated by the high temperatures.

Based on the above discussion, at the instant of detonation pressures of at least 8 GPa and temperatures of >8000 K occurred in the fireball. Air was driven away from ground zero and arkosic sand was entrained in the fireball upon the collapse of the detonation bubble. This sand underwent heterogeneous melting producing a variety of liquids. The larger liquid droplets formed the trinitite rain that led to the trinitite glass layer in the immediate vicinity of ground zero. Smaller droplets were transported away from the site forming spherical and dumbbell shaped droplets (Fig. 11). As is evident from the textures described previously, the liquids quickly quenched to glass and there was little mixing between the various liquid components. However, the flow structures that are common in the trinitite fragments are evidence of fluid behavior that occurred before final solidification.

Viscosity of trinitite liquids. The viscosity of the trinitite liquids at various temperatures was determined using the model developed by Grundy et al (2008a,b), Brosh et al. (2012a,b), Kim et al. (2012a,b), and Kim et al. (2013). The viscosity values were calculated using FactSage software (Bale et al. 2009) and the results are given in electronic Appendix II. Supplementary Data Table and shown graphically on Fig. 12. For all the glass compositions we calculated the viscosity at 1700 ^{o}C which obviously represents an instant in the cooling history of the trinitite liquid. Variations in Fe and Si have the greatest impact on the viscosities of silicate melts (Fig. 12a, b). For the high-Si liquid (the glass is mapped as quartz on the QEMSCAN® images) the

367 calculated viscosities at 1700 ^{o}C fall between 10^{5} and 10^{6} Pa·s. The lower silica glasses have
368 calculated viscosities ranging from $10^{-0.5}$ to 10^{2} Pa·s. The Fe-rich silicate glass has a calculated
369 viscosity of ~10^{-1} Pa·s. The Pb-rich silicate glasses have calculated viscosities of 1 - 10 Pa·s. On
370 the QEMSCAN® images we distinguish a number of chemical groups. The viscosity of the Fe-
371 rich glasses diverges from that of the other glasses (Fig. 12a). For the lower-Si compositional
372 groups, each group has a distinct range of viscosities which is essentially determined by the silica
373 content (Fig. 12b). For comparison purposes the calculated viscosities for the trinitite bead and
374 dumbbell are also plotted. The trinitite bead shows a greater range in Si, but the calculated
375 viscosities fall in the same range as the glasses.
376 The calculated viscosities for the four major glass groups are plotted as a function of
377 temperature on Figure 12c. The high-Si and low-Si glasses form two groups with the high-Si
378 glass having significantly greater viscosities above 800 ^{o}C. The three low-Si glasses show
379 similar viscosity trends as a function of temperature, but the trends are offset because of the
380 different SiO_2 content of the glasses. With decreasing temperature the viscosity contrast between
381 the low-Si glasses increases. As is clearly shown on the SEM images, significant mixing of the
382 liquids did not occur. Discrete bands and layers are shown on all the images. One possible
383 explanation for this lack of mixing is that while the various low-Si liquids had similar densities,
384 the differences in viscosity inhibited mixing. Where residual quartz and/or feldspar grains are
385 found in the glass (Figs. 5, 6) the layers wrap around the grains. Where orientation can be
386 determined (Fig. 5) the layers are more or less parallel to the land surface except when mineral
387 grains are present.
388 Let us consider the trinitite "rain" which consists of individual droplets of varying
389 composition determined by the specific mixtures of source material that formed a droplet. As the

rain impacts the surface it cools relatively quickly and there is a significant increase in viscosity (Fig. 12c). The rapid increase in viscosity would inhibit mixing between the liquids and the individual droplets would tend to flatten perpendicular to the gravitational direction or wrap around solid grains. In this scenario the partial melting textures shown, for example in Figures 5, 6, and 10, would be largely due to melting that took place while the droplets were airborne. The beads and dumbbells (Fig. 11) provide an insight into this process. In the bead we see diffuse areas of completely melted quartz grains and in the dumbbell we see partially melted quartz grains at the thicker end. In these examples the melting of quartz most certainly took place in the liquid droplets. We also see some flow banding in the dumbbell which is due to the airborne transport which caused elongation of the liquid droplet.

In the case of the red trinitite there are regions of high-Fe and high-Pb silicate glass. Liquids of these compositions would obviously be significantly denser than the normal silicate liquids. For the high-Fe silicate glass (at 1700 ^{o}C) the calculated liquid viscosity is ~10^{-1} Pa·s and for the high-Pb silicate glass the calculated liquid viscosity is 1 - 10 Pa·s . The SEM images (Figs. 7, 8) confirm that the Fe-rich and Pb-rich liquids readily flowed relative to the surrounding silicate liquids.

Geochemistry and petrology

Silicate glasses. The complete set of silicate glass compositions is found in electronic Appendix II. Supplemental Data. The data are summarized in a set of Harker diagrams (Fig. 13). The arkosic sand that served as the raw material for the trinitite glass is largely composed of quartz, plagioclase (albite), K-feldspar (microcline), muscovite, amphibole (actinolite according to XRD analysis, hornblende has also been reported), pyroxene, carbonates (caliche and occasional fossil fragments) and rock fragments. Barite, ilmenite, gypsum, and other minerals are

found in trace amounts. Fluid inclusion gas analysis of trinitite revealed a high concentration of CO_2 and an O_2/Ar ratio lower than the atmospheric ratio (Blamey et al. 2010).

As previously noted there are two major types of trinitite glasses – high-Si glass (essentially pure SiO_2) and a second lower-Si glass (SiO_2 varies from 55 to 80 wt.%). The high-Si glass comprises between 17 and 32 vol% of the trinitite. Because the chemistry of the melted and unmelted material in the high silica category is similar, it cannot be differentiated using QEMSCAN® analysis. Hence, the high silica category does include some unmelted and partially melted quartz grains. The composition of this material will not be considered further as it is essentially pure SiO_2.

With several notable exceptions the chemistry of the lower-Si trinitite glass can be represented as a mixture of the various mineral phases found in the arkosic sands. On the Harker diagrams (Fig. 13) fields have been constructed using quartz, muscovite, microcline and actinolite as end member compositions and in the case of the CaO-SiO_2 plot, anorthite to represent the Ca-plagioclase end member. The Fe Ca Al silicate glass falls outside the mineralogically defined fields undoubtedly due to the addition of anthropogenic iron. The three compositionally dominant glasses as mapped by QEMSCAN® (Table 1) are Ca Al silicate glass, Al Ca K silicate glass, and Ca Al K silicate glass. On most of the Harker diagrams the three major glass groups plot in separate areas and their chemistry can be explained as a mixture of the various silicate minerals. The notable exception is Ca which requires a carbonate component. For the Ca Al silicate glass group note the roughly linear trend extending from albite toward calcite (Fig. 13).

In order to quantify these observations linear mixing calculations were made for the major glass composition groups and potential mineral components (Table 5). In all the glasses

quartz is a minor component (6 – 23 wt%) relative to the quartz content of the arkosic sand. This suggests that much of the melted quartz formed a high silica liquid that did not mix with the other major compositional liquids, in agreement with the QEMSCAN® data that "quartz" glass is a major component of trinitite. For the relatively high Ca glasses calcite is a significant component comprising up to 26 wt% of the glass. The two relatively Fe-rich glasses, Fe Ca Al silicate and Ca Al Fe silicate, cannot be explained by simple mixing of the mineral components (calculations not reported). Both of these glasses require the addition of iron, probably as an anthropogenic component. The trinitite bead and dumbbell have similar compositions to the trinitite fragments.

The variety of glass compositions seen in trinitite can be explained as simple mixtures of melted mineral components. However, none of these mixtures represent equilibrium melting. Given the original starting material (arkosic sand) minimum granitic melt compositions might be expected. However projection of the compositional data (not shown) into the low pressure SiO_2-K_2O-Na_2O diagram reveals that none of the glasses approximate minimum melts. The liquids which formed the trinitite glasses were the result of disequilibrium melting of various mineral phases and the liquid compositions were maintained during the ensuing rapid quenching. There was little mixing between the various liquids. One conclusion is that the various stringers observed in the BSE's represent individual droplets of silicate liquid that were flattened and underwent minor flow during deposition of the "trinitite rain". Even in the case of the beads and dumbbells individual melted droplets maintained their compositional integrity during airborne transport.

Metallic phases. In Table 1 the QEMSCAN® modal data was combined into broad groups for simplicity of presentation and interpretation. The underlying data is much more

459 detailed (Appendix II. Supplementary Data Table) and here we consider this more detailed data
460 for the metallic phases (Table 6). Fahey et al. (2010) noted the presence of Fe-rich spheres in the
461 trinitite glass and on the walls of vesicles. In an SEM study Bellucci and Simonetti (2012) found
462 Fe-Si, Fe-Ti, Cu-S, and PbO spherules. They also identified a single grain of a W-Ga-Ta alloy.
463 Most of these inclusions were found on vesicle walls leading Bellucci and Simonetti (2012) to
464 conclude that the spherules were late additions to the trinitite layer.

465 Copper is found in many of the trinitite samples but the highest concentrations (by an
466 order of magnitude or greater) are found in red trinitite. Copper occurs in three associations –
467 with silicates, with sulfur, and less commonly as Cu metal. The Cu silicate association is most
468 common and is found in both red and green trinitite, although it is much more abundant in red
469 trinitite. The Cu-S and Cu metal association is essentially confined to red trinitite. The paucity of
470 Cu sulfides in the green trinitite is puzzling because the most likely source of sulfur would be
471 gypsum which is found in the arkosic sands. If this were the case then one might expect that Cu
472 sulfides would occur in all glasses. It is tempting to speculate that this may be due to the redox
473 state and that the environment in which the red trinitite liquids formed was more reducing than
474 that of the green trinitite liquids.

475 Iron occurs as iron oxide and metallic iron in blebs and as dendrites (Fig. 9). There are
476 also regions of Fe-rich silicate glass (Fig. 8). Given the high Fe content of the glass it is possible
477 that liquid immiscibility existed between the Fe-rich silicate liquid and the normal silicate liquid.
478 The compositions of the Fe-rich silicate glass and the normal silicate glass are compared to
479 experimental immiscible melts from common tholeiitic systems using the diagram (Fig. 14)
480 developed by Kamenetsky et al. (2013). The compositions fall on the liquid-liquid miscibility
481 gap. The width of the immiscibility field is a function of temperature and the compositions of the

482 inferred conjugate liquids correspond to an equilibration temperature of ~980°C. An important
483 caveat is that the experimental systems contained significant phosphorus, while the phosphorus
484 content of the trinitite glasses is less than 0.1 wt% P_2O_5 (less than the detection limit for P_2O_5
485 which is 0.1 wt%). There is a sharp boundary between the Fe-rich silicate glass and the normal
486 silicate glass as shown on Fig. 8c, d. In Figure 8c the slightly brighter region that occurs between
487 the high-Fe silicate glass and the normal silicate glass is due to the higher Pb content (Table 4,
488 analysis RTL4). Thus the chemical and observational data are consistent with the inference that
489 the Fe-rich silicate glass and the normal silicate glass may represent quenched immiscible
490 liquids.

491 Lead occurs in several associations – Cu-S-Pb-Si, Cu-Fe-S-Pb, and Pb-S-Si. Fig. 9a
492 illustrates the Cu-Fe-S-Pb association. The host material appears to be copper, containing both
493 large and small iron spherules and irregular lead-rich regions. We interpret these features as
494 evidence of immiscibility between the various metal phases. Fig. 9d illustrates the occurrence of
495 small Pb- rich blebs in a larger Fe-rich globule.

496 Mossbauer spectroscopy of trinitite glass (Sheffer and Dyar 2004) indicates that the iron
497 is largely in the +2 state. This is in accord with our other data regarding the presence of metallic
498 iron and copper and iron metal and sulfides, plus the red color of the red trinitite glass which
499 suggests that the copper is reduced. Hence all the observational and chemical data lead to the
500 conclusion that the trinitite melts formed and solidified in a reducing environment.

501 **Fulgurites, tektites, and trinitite**

502 Fulgurites (formed by lightning strikes), tektites (formed by meteorite impact), and
503 trinitite (formed by an atomic explosion) are all the result of high-temperature short duration
504 events. Temperature estimates vary widely and are often based on the melting behavior of quartz

505 which leads to the conclusion that temperatures exceeded 1700 ^{o}C because quartz grains are
506 either partially or totally melted (for example, tektites, Bunch et al. 2012). In complex systems,
507 as represented by melted rock material, quartz will melt at temperatures significantly less than
508 the melting temperature of pure quartz and this introduces some uncertainty into the temperature
509 estimates. Belkin and Horton (2009) investigated the petrography of melt-rich suevite from the
510 Chesapeake Bay impact structure. Utilizing the occurrence or absence of certain minerals and
511 their polymorphs they determined a range of melt temperatures and pressures for the various
512 glass phases with a maximum temperature of ~2000 ^{o}C and a maximum pressure of ~4-6 GPa.
513 Essene and Fisher (1986), using thermodynamic calculations based on the presence of coexisting
514 metallic and silicate liquids, arrived at a temperature of greater than 1750 ^{o}C for the formation
515 temperature of a fulgurite. Initial temperatures for the Trinity explosion were estimated to be in
516 excess of 8000 ^{o}C, but the mineralogical relations indicate much lower melting temperatures.
517 Quartz is present as discrete grains, often showing crenulate margins with the surrounding glass
518 (Fig. 10) and there are regions of pure silica glass which maintain the outlines of the initial
519 quartz grains. Thus temperatures were not above 1800 ^{o}C for a sufficiently long time to allow
520 complete melting of quartz. Where quartz and feldspar grains are in contact (Fig. 6) there is a
521 small region of glass between the grains. This particular situation approximates a binary system
522 and the eutectic melting temperature is ~990 ^{o}C (Schairer and Bowen 1955). This temperature is
523 in agreement with the equilibration temperature (~980 ^{o}C) for the inferred immiscible Fe-rich
524 and normal silicate liquids. Fulgurites, tektites, and trinitite all exhibit similarly complex melting
525 histories with maximum temperatures probably exceeding 2000 ^{o}C, but these maximum
526 temperatures were of short duration. Many of the observed mineralogical and petrological

relationships indicate that melting occurred at lower temperatures, perhaps during the cooling history of the initial liquid.

Neutron diffraction analysis of quartz in a Sahara fulgurite yields a shock pressure of ~25 GPa (Ende et al. 2012). Based on the occurrence of high pressure mineral polymorphs, planar deformation features and other indicators of shock metamorphism pressures of up to 50 – 100 GPa have been determined for impact events (French 1998). During the formation of the trinitite liquids we estimate that pressures were at least 8 GPa. High pressures are more significant in the formation of tektites, less so for fulgurites, and least for trinitite where temperature was the major factor.

The other characteristic shared by fulgurites, tektites, and trinitite is reducing conditions. Based on the occurrence of coexisting silicate and metallic melts in a fulgurite, Essene and Fisher (1986) estimated that the oxygen fugacity fell between the SiO_2-Si and FeO-Fe buffers. For a temperature of 1727 ^{o}C the resulting $f[O_2] = 10^{-15}$ to 10^{-8}. Mössbauer spectroscopic studies have indicated that fulgurites and trinitite formed under similar oxygen fugacities. The presence of immiscible sulfide melts and the predominance of Fe^{2+} in tektites (Belkin and Horton 2009) suggests that tektites are also formed under reducing conditions.

IMPLICATIONS

The Trinity site has been the focal point of a number of scientific investigations largely because of its historical significance as the location of the first atomic bomb test. However, the observations and interpretations derived from trinitite are universally applicable to glasses produced by other high temperature short duration events (whether of natural or human cause). The advantage of studying glasses from the Trinity site is that we have some knowledge of the conditions of formation; maximum temperature of ~8400 K, relatively high pressures (at least 8

GPa), and a duration of 14 to 20 s with the maximum temperatures associated with the fireball existing for ~3 s. Also formed during the same "experiment" were glass beads and dumbbells that are morphologically, physically and chemically similar to tektites. The temperature proxies associated with the trinitite glass, such as the presence of only partially melted quartz and feldspar grains, coexisting Fe-rich and Fe-poor silicate glass (originally liquids), and unmixing textures observed in metallic droplets, all point towards lower temperatures for the event. In terms of pressure, the presence of PDFs in some quartz grains suggests relatively high pressures (at least 8 GPa) but XRD studies reveal that the quartz is low temperature – low pressure α-quartz. Thus the mineralogical and petrological evidence found in the trinitite glasses indicate lower pressure and temperature conditions than actually existed and most likely represent a snapshot of the cooling history of the liquids. The short duration of the event precludes complete melting and equilibration and thus the mineralogical evidence may significantly underestimate the maximum temperature, a caveat that is equally applicable to trinitite, tektites and fulgurites.

Because of the short duration of the event, the trinitite glasses are extremely heterogeneous at the 10s of μm scale. The combination of conventional SEM back-scattered-electron images and chemical compositions derived from the QEMSCAN® analysis is a powerful tool for delineating these heterogeneities. The BSE images are generally more suitable for revealing textural variations while the QEMSCAN® images, and accompanying quantitative data about modal proportions, show the chemical variations. The ability to form compositional groups (QEMSCAN®) allows one to clearly identify areas of similar glass composition. We would suggest that any study that attempts to look at variations in parameters such as radioactivity and/or trace elements that might be used for forensic investigations, or other purposes, should be

572 preceded by a BSE-QEMSCAN® analysis such as was done in this study. This will ensure that
573 one is analyzing similar material.

574 ## ACKNOWLEDGMENTS

575 We are most thankful to the US Army White Sands Missile Range Public Affairs Office
576 personnel (Jim Eckles, Monte Marlin, Lisa Blevins, Cammie Montoya, and Debbie Bingham)
577 who allowed the collection of the various types of trinitite samples used in this study, for without
578 their cooperation, this work could not be performed. The Trinity Site, a National Historic
579 Landmark, is open to the general public once a year, the first Saturday in April. Pierre Hudon
580 and an anonymous reviewer are thanked for their comments which greatly improved the
581 manuscript and we thank Don Baker for his editorial assistance. Pierre Hudon, McGill
582 University, provided the FactSage viscosity calculations.

583 ## REFERENCES CITED

584 Armitage, P.J., Worden, R.H., Faulkner, D.R., Aplin, A.C., Butcher, A.R., and Espie, A.A.
585 (2013) Mercia Mudstone Formation caprock to carbon capture and storage sites:
586 petrology and petrophysical characteristics. Journal of the Geological Society, London,
587 170, 119-132.
588 Bale, C.W., Bélisle, E., Chartrand, P., Decterov, S.A., Eriksson, G., Hack, K., Jung, I.H., Kang,
589 Y.B., Melancon, J., Pelton, A.D., Robelin, C., and Petersen, S. (2009) FactSage
590 thermochemical software and databases – recent developments. Calphad, 33, 295-311.
591 Belkin, H.E., and Horton, J.W., Jr. (2009) Silicate glasses and sulphide melts in the ICDP-USGS
592 Eyreville B core, Chesapeake Bay impact structure, Virginia, USA. In G.S. Gohn, C.
593 Koeberl, K.G. Miller, and W.U. Reimold, Eds, the ICDP-USGS deep drilling project in

the Chesapeake Bay impact structure: results from the Eyreville core holes, vol. 458, p. 447-468. Special Paper, Geological Society of America, Boulder.

Belloni, F., Himbert, J., Marzocchi, O., and Romanello, V. (2011) Investigating incorporation and distribution of radionuclides in trinitite. Journal of Environmental Radioactivity, 102, 852-862.

Bellucci, J.J., and Simonetti, A. (2012) Nuclear forensics: searching for nuclear device debris in trinitite-hosted inclusions. Journal of Radioanalytical and Nuclear Chemistry, 293, 313-319.

Bellucci, J.J., Wallace, C., Koeman, E., Simonetti, A., Burns, P., Keser, J., Port, E., and Walczak, E. (2013) Distribution and behavior of some radionuclides associated with the Trinity nuclear test. Journal of Radioanalytical and Nuclear Chemistry, 295, 2049-2057.

Blamey, N.J.F., Boslough, M.B., Newsom, H., and Parnell, J. (2010) Quantitative fluid inclusion gas analysis of airburst, nuclear, impact, and fulgurite glasses. Geological Society of America Abstracts with Programs, 42, 5, 305.

Brosh, E., Pelton, A.D., and Decterov, S.A. (2012) A model to calculate the viscosity of silicate melts. International Journal of Materials Research, 103, 494-501.

Brosh, E., Pelton, A.D., and Decterov, S.A. (2012) A model to calculate the viscosity of silicate melts. International Journal of Materials Research, 103, 537-550.

Bunch, T.E., Hermes, R.E., Moore, A.M.T., Kennett, D.J., Weaver, J.C., Wittke, J.H., DeCarli, P.S., Bischoff, J.L., Hillman, G.C., Howard, G.A., Kimbel, D.R., Levtetschka, G., Lipo, C.P., Sakai, S., Revay, Z., West, A., Firestone, R.B., and Kennett, J.P. (2012) Very high-temperature impact melt products as evidence for cosmic airbursts and impacts 12,900 years ago. Proceedings of the National Academy of Sciences, 109, 28, E1903-E1912.

Burton, B. (1991) The Fe-Pb (iron-lead) system. Journal of Phase Equilibria, 12, 200-202.

Eby, G.N., Charnley, N., and Smoliga, J. (2010a) Trinitite – the atomic rock. Geological Society of America Abstracts with Programs, 42, 1, 77.

Eby, G.N., Hermes, R., Charnley, N., and Smoliga, J. A. (2010b) Trinitite – the atomic rock. Geology Today, 26, 181-186.

Ende, M., Schorr, S., Kloess, G., Franz, A., and Tovar, M. (2012) Shocked quartz in Sahara fulgurite. European Journal of Mineralogy, 24, 499-507.

Essene, E.J., and Fisher, D.C. (1986) Lightning strike fusion: extreme reduction and metal-silicate liquid immiscibility. Science, 234, 189-193.

Fahey, A.J., Zeissler, C.J., Newbury, D.E., Davis, J., and Lindstrom, R.M. (2010) Postdetonation nuclear debris for attribution. Proceedings of the National Academy of Sciences, 107, 20207-20212.

French, B.M. (1998) Traces of catastrophe: A handbook of shock-metamorphic effects in terrestrial meteorite impact structures, 120 p., LPI Contribution 954, Lunar and Planetary Institute, Houston, Texas.

Glass, B.P., Senftle, F.E., Muenow, D.W., Aggrey, K.E., and Thorpe, A.N. (1987) Atomic bomb glass beads: tektite and microtektite analogs. Second International Conference on Natural Glasses, Prague, 361-369.

Gratz, A.J., Fisler, D. K., and Bohor, B. (1996) Distinguishing shocked from tectonically deformed quartz by the use of the SEM and chemical etching. Earth and Planetary Science Letters, 142, 513-521.

Grundy, A.N., Liu, H., Jung, I-H., Decterov, S.A., and Pelton, A.D. (2008) A model to calculate the viscosity of silicate melts: Part I. Viscosity of binary SiO_2#x2013, MeOx systems (Me = Na, K, Ca, Mg, Al). International Journal of Materials Research, 99, 1185-1194.

Grundy, A.N., Liu, H., Jung, I-H., Decterov, S.A., and Pelton, A.D. (2008) A model to calculate the viscosity of silicate melts: Part II. The $NaO_{0.5}$-MgO-CaO-$AlO_{1,5}$-SiO_2 system. International Journal of Materials Research, 99, 1155-1209.

Hermes, R.E., and Strickfaden, W.B. (2005) A new look at trinitite. Nuclear Weapons Journal, 2, 2-7.

Kamenetsky, V.S., Charlier, B., Zhitoba, L., Sharygin, V., Davidson, P., and Feig, S. (2013) Magma chamber-scale liquid immiscibility in the Siberian Traps represented by melt pools of native iron. Geology, 41, 1091-1094.

Kim, W.Y., Pelton, A.D., and Decterov, S.A. (2012) A model to calculate the viscosity of silicate melts. International Journal of Materials Research, 103, 313-328.

Kim, W.Y., Pelton, A.D., and Decterov, S.A. (2012) Modeling the viscosity of silicate melts containing lead oxide. Metallurgical and Materials Transactions B, 43, 325-326.

Kim, W.Y., Pelton, A.D., Bale, C.W., Bélisle, E., and Decterov, S.A. (2013) Modeling the viscosity of silicate melts containing manganese oxide. Journal of Mining and Metallurgy B: Metallurgy, 49, 323-337.

Koeberl, C. (1997) Impact cratering: the mineralogical and geochemical evidence. In K.S. Johnson and J.A. Campbell, Eds., Ames structure in northwest Oklahoma and similar features: origin and petroleum production, p. 30-54. Oklahoma Geological Survey Circular 100, Norman, Oklahoma.

Kretz, R. (1983) Symbols for rock-forming minerals. American Mineralogist, 68, 277-279.

Onderka, B., Jendrzejczyk-Handzlik, D., and Fitzner, K. (2013) Thermodyanmic properties and phase equilibria in the ternary C-Pb-Fe system. Archives of Metallurgy and Materials, 58, 541-548.

Parekh, P.P., Semkow, T.M., Torres, M.A., Haines, D.K., Cooper, J.M., Rosenberg, P.M., and Kitto, M.E. (2006) Radioactivity in trinitite six decades later. Journal of Environmental Radioactivity, 85, 103-120.

Pirrie, D., and Rollinson, G.K. (2011) Unlocking the application of automated mineralogy. Geology Today, 27, 226-235.

Pirrie, D., Butcher, A.R., Power, M.R., Gottlieb, P., and Miller, G.L. (2004) Rapid quantitative mineral and phase analysis using automated scanning electron microscopy (QEMSCAN®); potential applications in forensic geoscience. In K. Pye and D. Croft, Eds, Forensic Geoscience, vol. 232, p. 123-136. Special Publication, Geological Society, London.

Pirrie, D., Power, M.R., Rollinson, G.K., Wiltshire, P.E.J., Newberry, J., and Campbell, H.E. (2009) Automated SEM-EDS (QEMSCAN®) mineral analysis in forensic soil investigations; testing instrumental variability. In K. Ritz, L. Dawson, and D. Miller, Eds., Criminal and Environmental Soil Forensics, p. 411-430. Springer, Berlin.

Potter, S.L., Chan, M.A., Petersen, E.U., Dyar, M.D., and Sklute, E. (2011) Characterization of Navajo Sandstone concretions: Mars comparison and criteria for distinguishing diagenetic origins. Earth and Planetary Science Letters, 301, 444-456.

Ross, C. (1948) Optical properties of glass from Alamogordo, New Mexico. American Mineralogist, 33, 360-361.

683 Sheffer, A.A., and Dyar, M.D. (2004) ^{57}Fe Mössbauer spectroscopy of fulgurites: implications
684 for chemical reduction. Lunar and Planetary Science XXXV, 1372.
685 Staritzky, E. (1950) Thermal effects of atomic bomb explosions on soils at Trinity and Eniwetok.
686 Los Alamos Scientific Laboratory, LA-1126, 16 pp.
687 Wang, C.P., Liu, X.J., Jiang, M., Ohnuma, I., Kainuma, R., and Ishida, K. (2005)
688 Thermodynamic database of the phase diagrams in copper base alloy systems. Journal of
689 Physics and Chemistry of Solids, 66, 256-260.

690 **FIGURE CAPTIONS**

691 **FIGURE 1.** Examples of trinitite glasses. (**a**) bottle green trinitite, (**b**) pancake trinitite, (**c**) red
692 trinitite collected north of ground zero.

693 **FIGURE 2.** Trinitite beads and dumbbells. Top reflected light, bottom transmitted light.

694 **FIGURE 3.** X-ray diffraction patterns. (**a**) trinitite beads and glass fragments, (**b**) Trinity
695 arkosic sand. Quartz, muscovite, albite, microcline and actinolite were identified in the arkosic
696 sand. Only α-quartz was found in the trinitite beads and glass fragments.

697 **FIGURE 4.** (**a**) Back scattered electrons (BSE) and (**b**) QEMSCAN® images for green trinitite
698 fragment BD3. Flow textures are well-developed. The green areas on the QEMSCAN® image are
699 partly digested K-feldspar grains. Note the irregular contact between K-feldspar and quartz in the
700 upper left corner of the image along which melting was occurring. The Ca Al silicate glass forms
701 a long stringer. The bulk of the sample consists of Al K Ca silicate glass. Numbered points are
702 spot analyses. The data are found in Table 2. Top half of the figure is modified from Eby et al.
703 (2010b), Fig. 12.

704 **FIGURE 5.** (**a**) BSE and (**b**) QEMSCAN® images for green trinitite fragment BD8. The
705 contact between the trinitite glass and the arkosic sand is shown at the top of the images. Flow

structures are well-developed and the flow lines deflect around the silica-rich regions. Chemical analyses are listed in Table 3.

FIGURE 6. (**a**) BSE and (**b**) QEMSCAN® images for green trinitite fragment BD11. Note reaction zone between large K-feldspar grain and the glass matrix. The bulk of the sample consists of an intimate mixture of Ca Al silicate and Ca Al K silicate glass. However note that in the SEM image flow banding is clearly defined and in the immediate vicinity of the K-feldspar grain the banding wraps around the K-feldspar.

FIGURE 7. BSE and QEMSCAN® images for red trinitite fragment RTS. (**a**) BSE image. The bright areas are metallic inclusions (From Eby et al. 2010b, Fig. 5b). (**b**) QEMSCAN® image, the colors correspond to different compositional groups. (**c**) Detailed image of area C. The dark gray regions are partially melted quartz grains. (**d**) Detailed image of area D. The bright areas have high Pb content. Chemical analyses for the various spots are listed in Table 4.

FIGURE 8. BSE and QEMSCAN® images for red trinitite fragment RTL. (**a**) BSE image. The bright areas are metallic inclusions. (**b**) QEMSCAN® image, the colors correspond to different compositional groups. (**c**) Detailed image of area C. #1 melted quartz grain, #2-4 Fe-rich silicate glass, and #5-6 silicate glass. (**d**) Detailed image of area D. #7 melted quartz grain, #8 Fe-rich silicate glass, and #9 silicate glass. Note the sharp contacts between the Fe-rich glass and the silicate glass. Chemical analyses for the various spots are listed in Table 4.

FIGURE 9. Metallic inclusions in red trinitite. I1 and I2 are from RTS and I3 and I4 are from RTL. See Figs. 7 and 8 for locations. (**a**) Fe blobs in a Cu/Pb matrix. The shape of the Fe blobs suggests that they were initially liquid droplets that were incorporated into a Cu/Pb liquid. Segregation of Cu and Pb liquids occurred with falling temperature (from Eby et al. 2010b, Fig. 5C). (**b**) Iron droplet with exsolved copper along the edges. (**c**) Cu/Fe droplet. Most likely this

729 was originally a mixture of Cu and Fe. With falling temperature the Fe began to exsolve. Also
730 note the occurrence of Fe dendrites, indicative of rapid cooling. In the Cu/Fe matrix the darker
731 areas are richer in Fe compared to the lighter areas which are richer in copper. (**d**) Iron droplet in
732 Cu/Fe matrix. The bright spots in the iron droplet are Pb. In the matrix the lighter areas are Cu
733 rich and the darker areas are Fe rich. The upper right portion of the image shows complex
734 unmixing between Cu and Fe liquids.

735 **FIGURE 10.** Thin section images of trinitite glass. Gypsum plate inserted to enhance contrast.
736 (**a**) Partially melted quartz grain showing glass embayments. (**b**) Linear features in quartz grain
737 interpreted as Planar Deformation Features (PDFs). These features are indicative of high
738 pressure.

739 **FIGURE 11.** Trinitite bead and dumbbell. (**a**) Trinitite bead with embedded melted quartz
740 grains (darker areas). (**b**) Trinitite dumbbell with embedded partially melted quartz grains
741 (darker areas). (**c**) Plane polarized light image of the trinitite dumbbell in B showing typical
742 bottle green color and flow banding. Image A is from Eby et al. (2010b) Fig. 10 and image B is
743 from Eby et al. (2010b) Fig. 11.

744 **FIGURE 12.** Plots of calculated viscosity versus FeO (**a**), SiO_2 (**b**), and temperature (**c**).

745 **FIGURE 13.** Glass compositions plotted on Harker diagrams. Mineral abbreviations are from
746 Kretz (1983). Shaded areas are for glass compositions that fall within the composition range of
747 the mineral end members.

748 **FIGURE 14.** Compositions of Fe-rich glass and normal silicate glass plotted on the
749 immiscibility diagram of Kamenetsky et al. (2013). $D\frac{SiO_2}{L_{Fe}/L_{Si}}$ is the partitioning of SiO_2 between
750 the iron-rich and silica-rich melts. Note that the trinity glasses contain negligible amounts of
751 phosphorus.

Table 1. Modal compositions derived from QEMSCAN data (Area%)

Sample Code	A	B	C	D
Sample Type	Red trinitite	Red trinitite	Green trinitite	Green trinitite
Measurement Mode	Field Image	Field Image	Field Image	Field Image
No. X-ray Analysis Points	1393661	2215645	5271929	3167255
X-ray Pixel Spacing (Microns)	5	5	5	5
Quartz	31.57	26.42	32.94	16.90
K-feldspar	6.07	8.01	7.94	3.09
Ca Al Silica glass	17.36	14.55	17.37	24.39
Al Ca K Silica glass	23.71	19.60	24.23	28.97
Ca Al Fe Silica glass	4.81	9.84	3.19	2.61
Ca Al K Silica glass	6.71	7.48	10.23	22.38
Fe Ca Al Silica glass	1.62	5.47	0.62	0.15
Ca Silica glass	3.33	5.01	2.72	1.18
Metal Phases	4.62	2.72	0.29	0.10
Others	0.23	0.91	0.49	0.24

752
753

Table 2. SEM spot analyses for green trinitite glass BD3 (wt%)

Sample	G1	G2	G3	G4	G5	G6	G7
SiO_2	51.3	53.5	53.7	73.4	69.5	68.2	66.9
TiO_2	0.33	0.26	0.40	0.36	0.21	0.27	0.42
Al_2O_3	14.3	15.5	15.0	12.5	14.3	14.8	13.9
FeO	2.62	2.17	2.53	1.67	1.23	1.31	2.04
MnO	0.01	0.09	0.04	0.02	0.01	0.01	0.08
MgO	1.55	1.22	1.50	0.96	0.76	0.91	1.09
CaO	25.3	20.9	20.9	4.52	5.13	5.93	10.0
Na_2O	1.84	1.86	1.86	1.96	2.12	2.49	1.78
K_2O	1.49	2.27	2.41	4.07	5.33	5.00	3.30
Total	98.7	97.8	98.3	99.5	98.6	98.9	99.5
Group	Ca Al	Ca Al	Ca Al	Al Ca K	Al Ca K	Al Ca K	Ca Al

754
755
756

Table 2. Continued

Sample	G8	G9	G10	G11	G12	G13	G14
SiO_2	63.3	63.6	68.9	62.5	71.6	65.2	69.0
TiO_2	0.33	0.23	0.37	0.29	0.30	0.21	0.28
Al_2O_3	17.6	17.4	14.6	16.5	12.8	14.1	14.5
FeO	1.62	1.32	1.46	2.01	1.35	1.68	1.31
MnO	0.05	0.01	0.02	0.01	0.03	0.01	0.02
MgO	1.06	0.59	0.80	1.18	0.63	0.92	0.78
CaO	7.22	6.30	5.14	9.78	4.59	9.77	5.19

Na_2O	3.14	3.06	2.29	2.25	2.08	1.85	2.42
K_2O	4.70	5.61	6.05	4.23	5.17	4.20	5.31
Total	99.0	98.1	99.6	98.8	98.6	97.9	98.8
Group	Ca Al K	Al Ca K	Al Ca K	Ca Al K	Al Ca K	Ca Al K	Al Ca K

757
758

Table 3. SEM spot analyses for green trinitite glass BD8 (wt%)

Sample	G1	G2	G3	G4	G5	G6	G7
SiO_2	70.7	66.4	68.0	75.5	66.2	66.4	61.3
TiO_2	0.37	0.52	0.39	0.22	0.68	0.58	0.38
Al_2O_3	11.7	13.5	13.5	9.31	13.3	13.9	11.6
FeO	2.16	2.60	2.40	2.00	2.94	2.62	2.14
MnO	0.06	0.14	0.07	0.08		0.02	
MgO	1.18	1.42	1.50	1.29	1.51	1.38	1.33
CaO	7.71	9.47	8.38	6.40	9.90	8.91	18.3
Na_2O	1.37	1.38	1.60	1.33	1.56	1.69	1.43
K_2O	3.67	3.55	3.56	3.66	3.29	3.66	2.64
Total	98.9	99.0	99.4	99.8	99.4	99.2	99.1
Group	Ca Al K	Ca Al K	Ca Al K	Al Ca K	Ca Al K	Ca Al K	Ca Al

759
760
761

Table 3. Continued

Sample	G7	G8	G9	G10	G11
SiO_2	61.3	58.0	65.2	62.6	67.8
TiO_2	0.38	0.41	0.43	0.48	0.45
Al_2O_3	11.6	11.0	11.9	12.6	12.8
FeO	2.14	2.49	2.23	2.55	2.19
MnO		0.12	0.09		0.03
MgO	1.33	1.44	1.17	1.42	1.29
CaO	18.3	22.3	13.2	15.3	9.04
Na_2O	1.43	1.24	1.76	1.43	1.84
K_2O	2.64	2.00	3.66	2.91	3.77
Total	99.1	99.0	99.6	99.3	99.2
Group	Ca Al	Ca Al	Ca Al K	Ca Al	Ca Al K

762
763

Table 4. SEM spot analyses for red trinitite glass (wt%)

Sample	RTS1	RTS2	RTS3	RTS4	RTS5	RTS6	RTS7
SiO_2	68.3	61.0	63.8	58.3	49.6	53.8	55.7
TiO_2	0.29	0.53	0.53	0.62	0.53	0.08	0.54

Al_2O_3	12.9	10.7	12.6	13.8	8.7	11.5	13.2
FeO	2.12	3.98	3.30	4.66	3.54	1.40	3.08
MnO	0.09	0.19	0.08	0.17		0.03	0.08
MgO	1.12	1.56	1.29	1.85	1.19	0.54	1.43
CaO	4.47	12.8	9.3	13.2	5.65	1.98	4.34
Na_2O	1.89	1.37	1.77	1.46	1.08	1.18	1.47
K_2O	5.04	2.86	3.29	2.27	4.05	5.77	6.00
CuO	0.23	0.35	0.22	0.52	0.41	0.39	0.35
PbO					23.9	21.4	11.0
Total	96.5	95.3	96.2	96.9	98.7	98.1	97.2

Table 4. Continued

Sample	RTL1	RTL2	RTL3	RTL4	RTL5	RTL6	RTL7	RTL8	RTL9
SiO_2	100.1	42.0	43.7	43.4	61.5	63.3	100.4	44.2	63.4
TiO_2		0.32	0.40	0.32	0.57	0.43	0.05	0.26	0.39
Al_2O_3	0.21	5.86	7.62	6.23	13.2	12.8	0.33	7.79	13.6
FeO	0.16	40.1	36.1	38.2	5.66	5.58		35.9	7.11
MnO	0.02	0.06	0.07	0.03	0.14	0.07		0.06	0.04
MgO	0.13	0.97	0.92	0.81	1.68	1.26	0.29	1.06	1.35
CaO		5.64	6.07	5.37	10.3	7.56		5.28	6.31
Na_2O		0.55	0.54	0.40	1.48	1.90		0.51	1.77
K_2O		1.22	1.37	1.45	2.76	3.83		1.48	3.75
CuO		0.12	0.16	0.04	0.22	0.32		0.18	0.88
PbO		0.18	0.26	0.51	0.32	0.20		0.32	0.27
Total	100.6	97.0	97.2	96.8	97.8	97.3	101.1	97.0	98.9

Table 5. Results of mixing calculations for trinitite glasses

Composition Group	Ca Al Sil	Ca Al Sil	Ca Al Sil	Al Ca K Sil	Al Ca K Sil	Al Ca K Sil	Ca Al K Sil
Sample	RTL G5	TB3	BD3 G1	RTS1	BD3 G4	BD3 G14	BD3 G11
Quartz	0.113	0.095	0.020	0.228	0.190	0.296	0.061
K-feldspar	0.276	0.261	0.213	0.377	0.387	0.311	0.365
Albite	0.336	0.258	0.430	0.274	0.328	0.293	0.417
Calcite	0.079	0.257	0.240	0.033	0.044	0.035	0.087
Actinolite	0.201	0.145	0.121	0.096	0.060	0.075	0.091
SSR	3.655	3.665	5.125	1.339	1.113	1.413	3.498

Values are proportion of each mineral component in the glass. SSR = Sum of the Squares Residual.

771

772

Table 6. Metallic phases in trinitite (Area%)

Sample Code	A	B	C	D
Sample type	Red trinitite RTS	Red trinitite RTL	Green trinitite	Green trinitite
Fe-Ox/CO3	0.685	0.747	0.086	0.026
Fe-Ox/CO3 (low Cu)	0.218	0.234	0.002	0.000
Cu Metal/Ox/CO3	0.504	0.451	0.006	0.007
Cu silicate	1.649	0.551	0.152	0.062
Ilmenite	0.004	0.004	0.004	0.000
Rutile	0.007	0.009	0.003	0.001
Titanite	0.026	0.023	0.006	0.002
Chalcopyrite	0.269	0.039	0.000	0.000
Cu sulphides	0.228	0.061	0.001	0.000
Cu-S-Pb-Si	0.134	0.061	0.000	0.000
Cu-Fe-S-Pb	0.122	0.073	0.000	0.000
Cu-S-Ca-Si	0.756	0.205	0.000	0.000
Pb-S-Si	0.052	0.304	0.043	0.000
Fe-S-Si	0.013	0.070	0.031	0.000
Zn oxide	0.003	0.006	0.001	0.001
Total	4.670	2.838	0.335	0.099

773

774

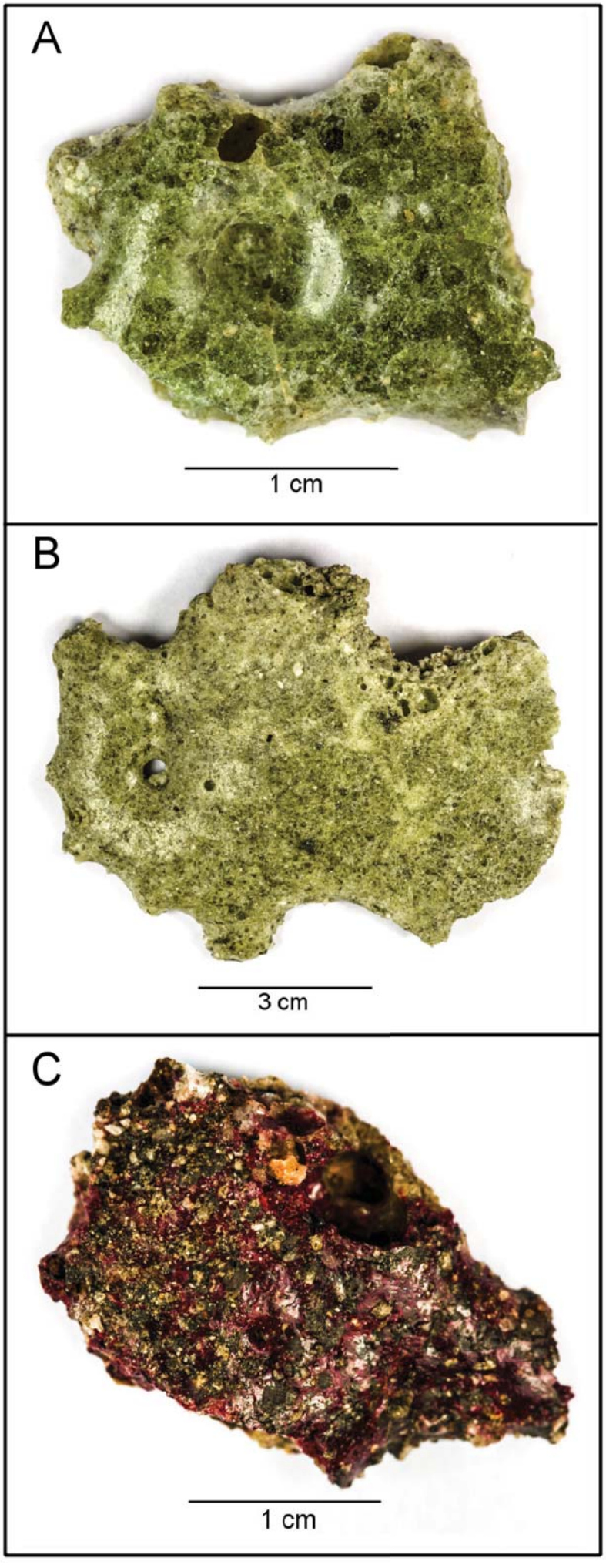

Figure 1

Figure 2

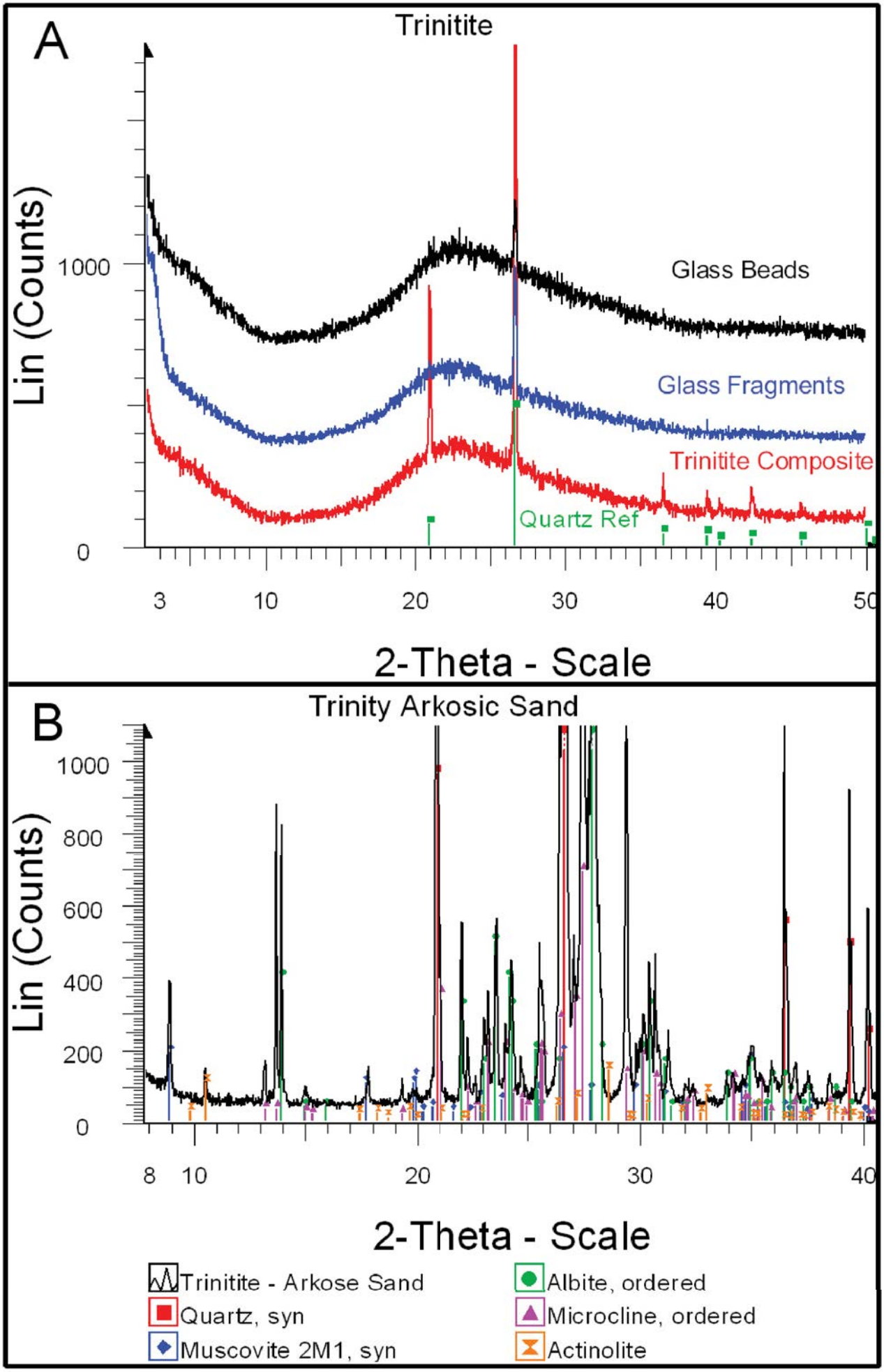
A
Trinitite
Lin (Counts)
1000
0
Glass Beads
Glass Fragments
Trinitite Composite
Quartz Ref
3
10
20
30
40
50
2-Theta - Scale
B
Trinity Arkosic Sand
Lin (Counts)
1000
800
600
400
200
0
8
10
20
30
40
2-Theta - Scale
Trinitite - Arkose Sand
Quartz, syn
Muscovite 2M1, syn
Albite, ordered
Microcline, ordered
Actinolite

Figure 3

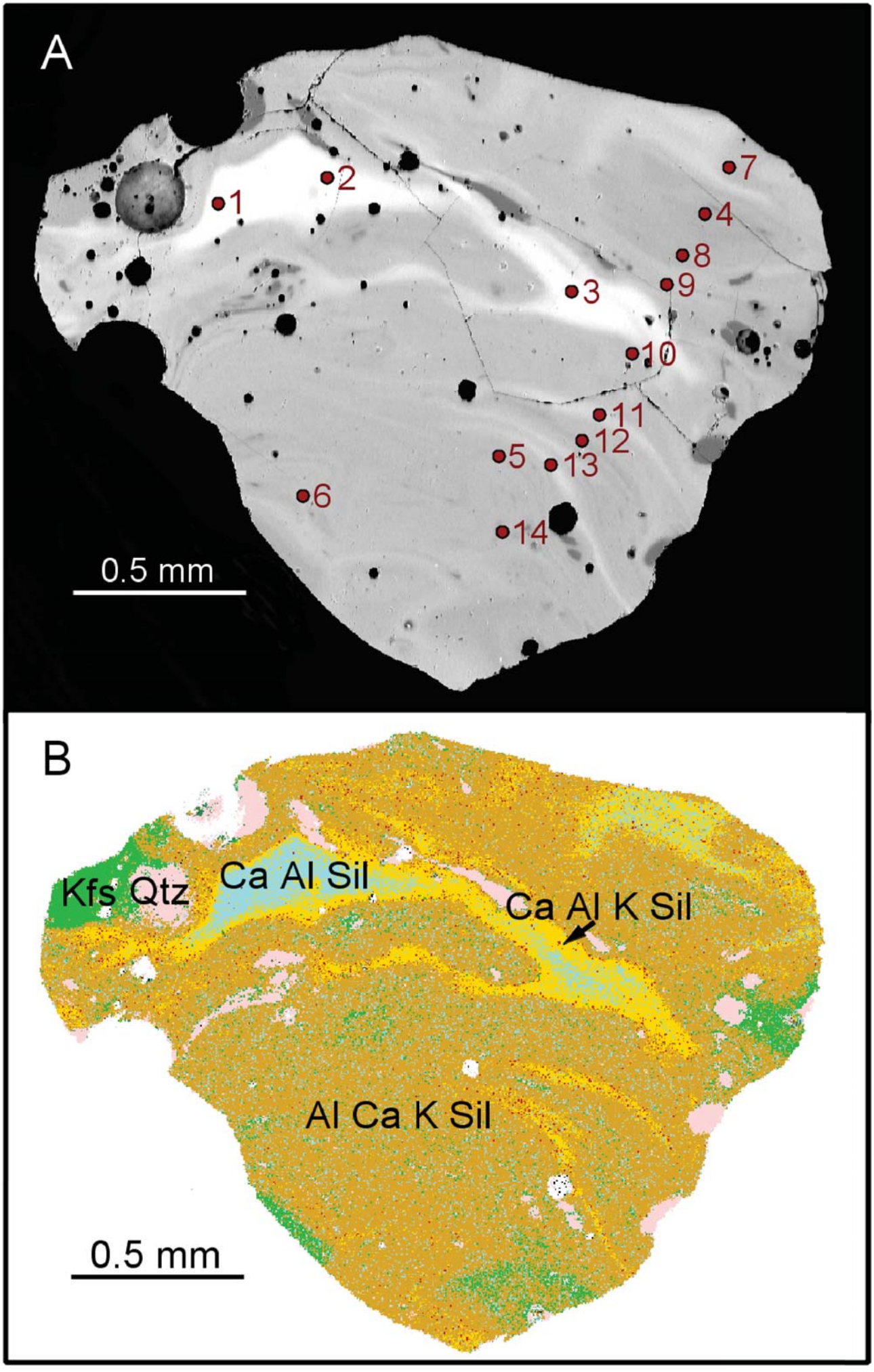
A
1
2
3
4
5
6
7
8
9
10
11
12
13
14
0.5 mm
B
Kfs Qtz
Ca Al Sil
Ca Al K Sil
Al Ca K Sil
0.5 mm

Figure 4

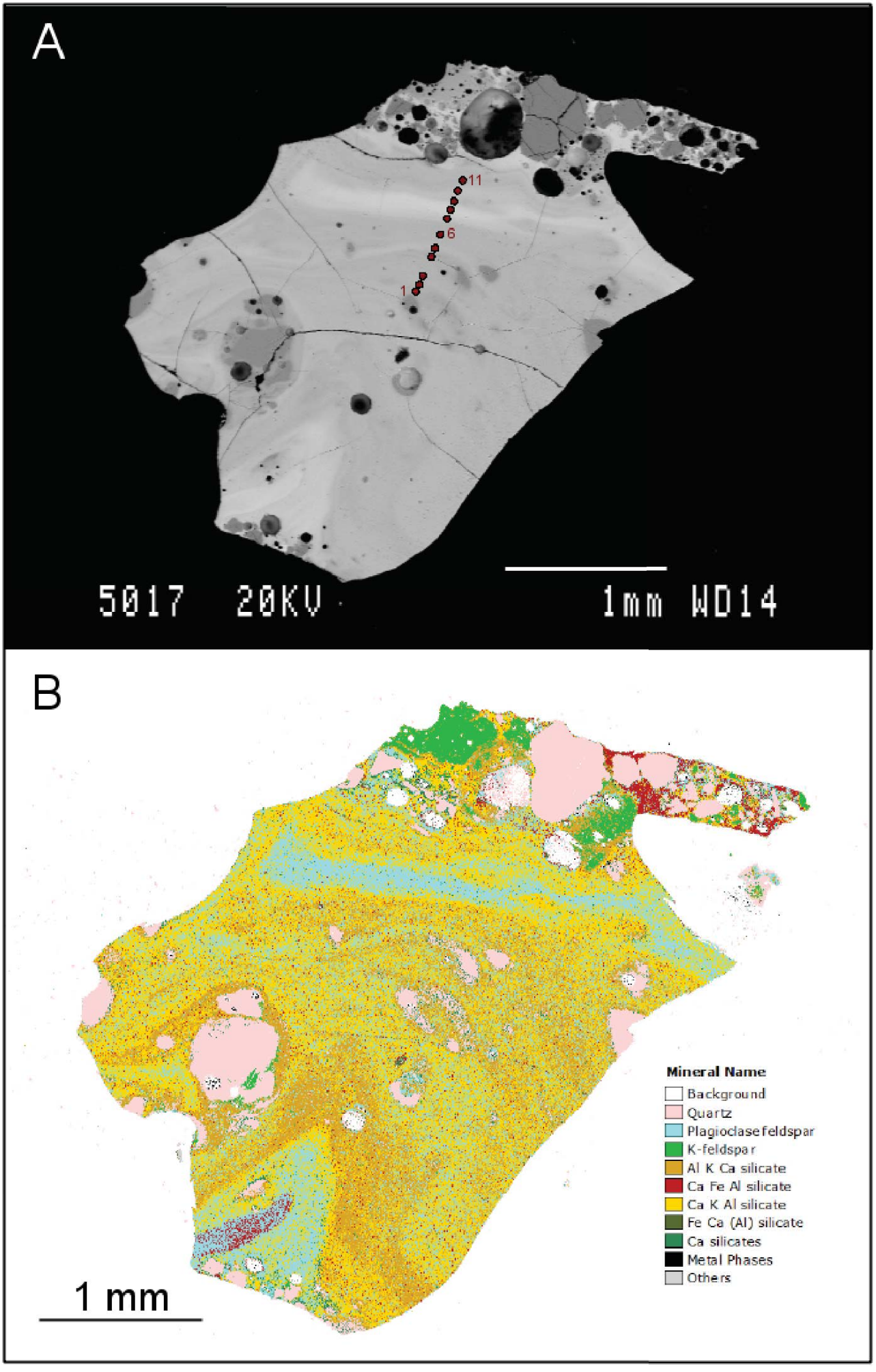
A
11
6
1
5017 20KV
1mm WD14
B
1 mm
Mineral Name
Background
Quartz
Plagioclase feldspar
K-feldspar
Al K Ca silicate
Ca Fe Al silicate
Ca K Al silicate
Fe Ca (Al) silicate
Ca silicates
Metal Phases
Others

Figure 5

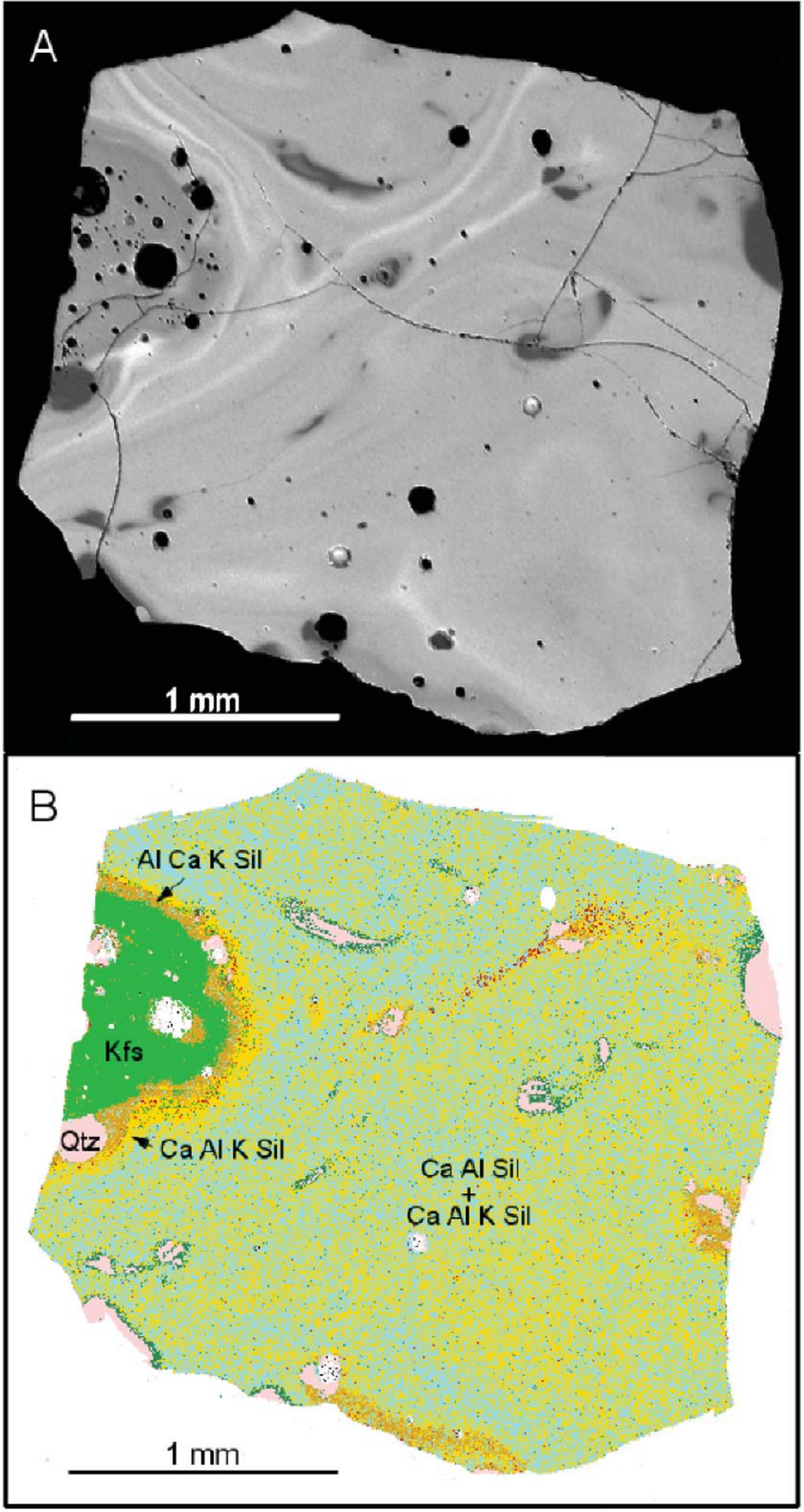

Figure 6

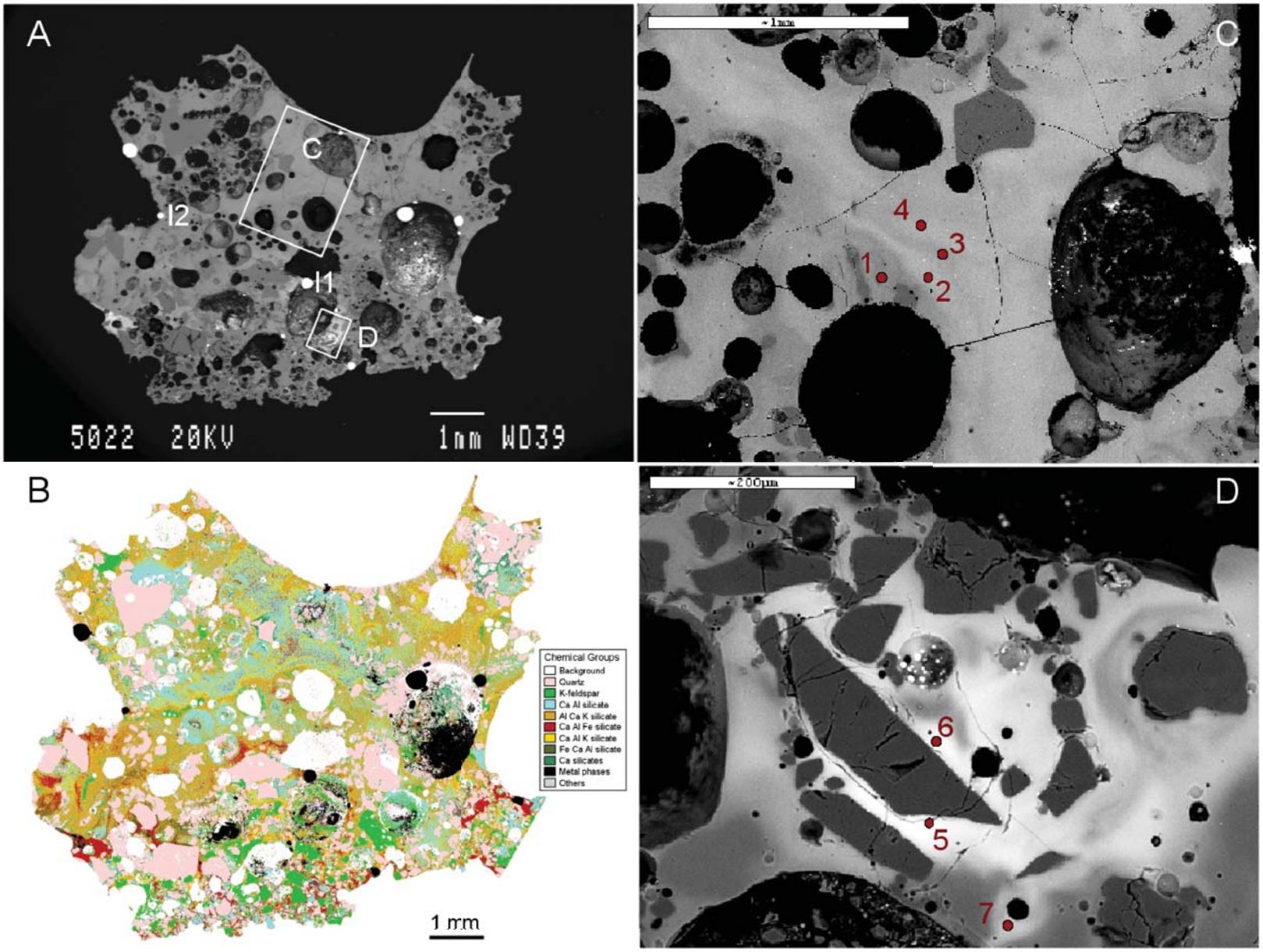
A
C
I2
I1
D
5022 20KV
1mm WD39
B
Chemical Groups
Background
Quartz
K-feldspar
Ca Al silicate
Al Ca K silicate
Ca Al Fe silicate
Ca Al K silicate
Fe Ca Al silicate
Ca silicates
Metal phases
Others
1 mm
C
1
2
3
4
D
5
6
7

Figure 7

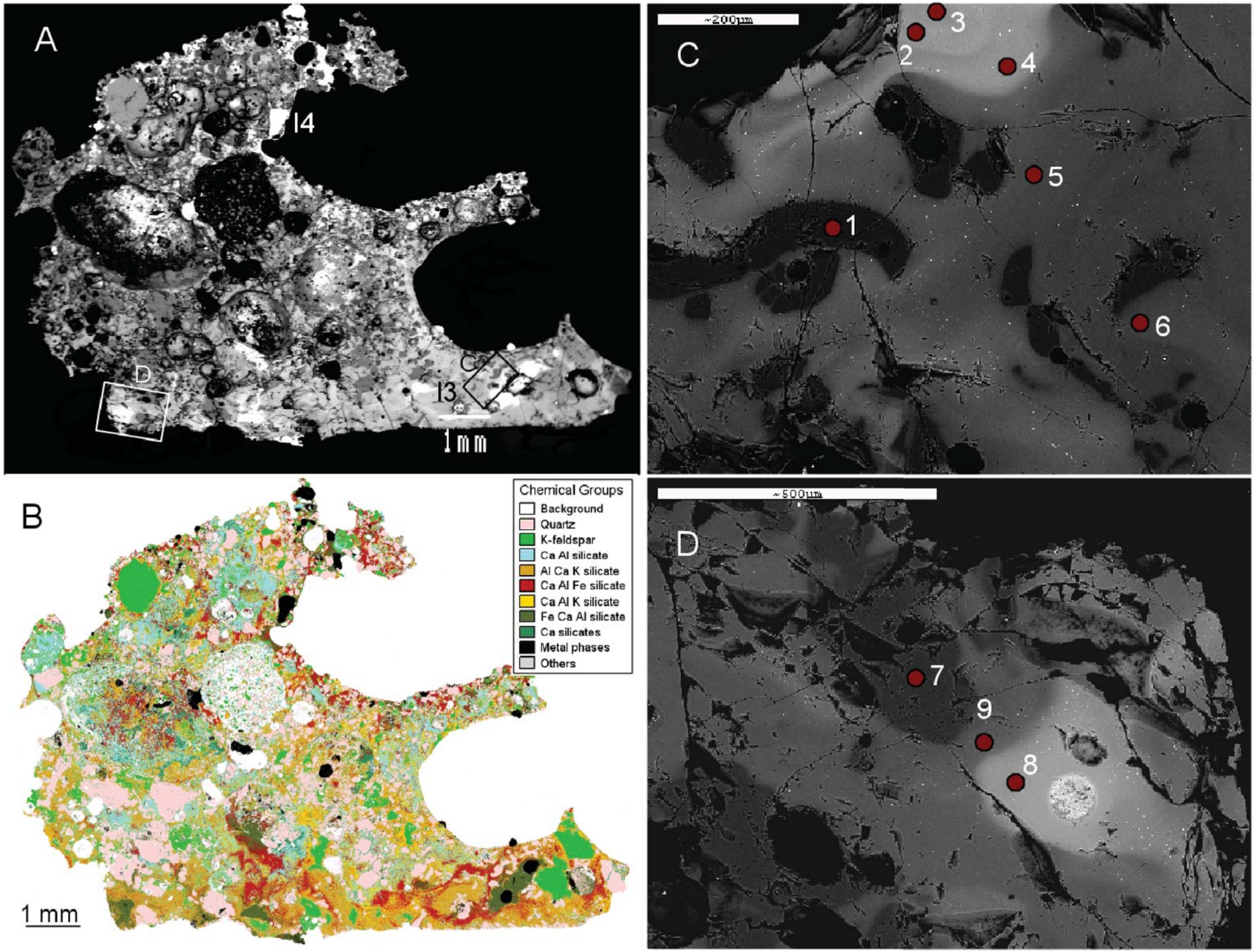
A
I4
I3
C
D
1 mm
B
Chemical Groups
Background
Quartz
K-feldspar
Ca Al silicate
Al Ca K silicate
Ca Al Fe silicate
Ca Al K silicate
Fe Ca Al silicate
Ca silicates
Metal phases
Others
1 mm
C
~200µm
1
2
3
4
5
6
D
~500µm
7
8
9

Figure 8

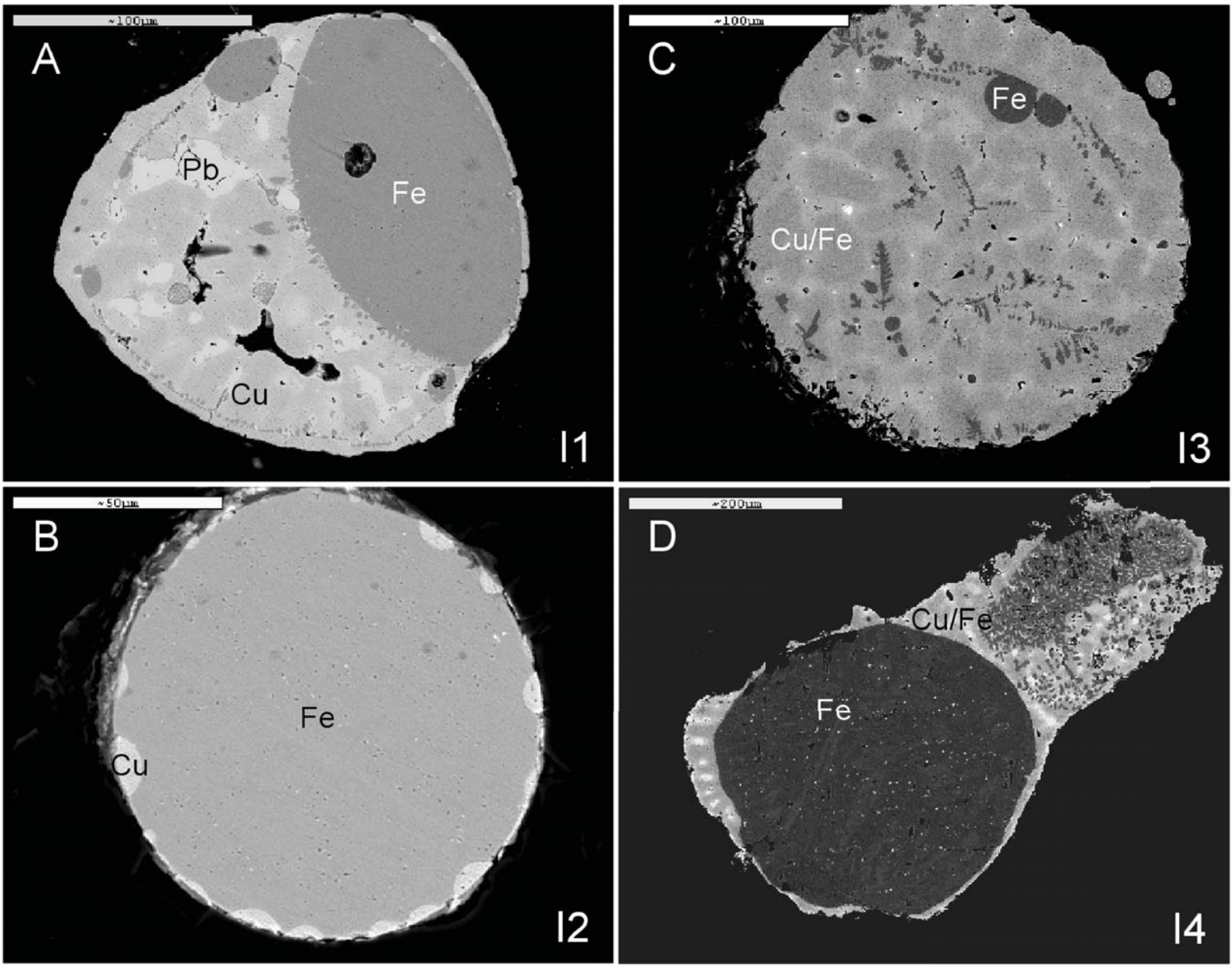
~100µm
A
Pb
Fe
Cu
I1
~100µm
C
Fe
Cu/Fe
I3
~50µm
B
Fe
Cu
I2
~200µm
D
Cu/Fe
Fe
I4

Figure 9

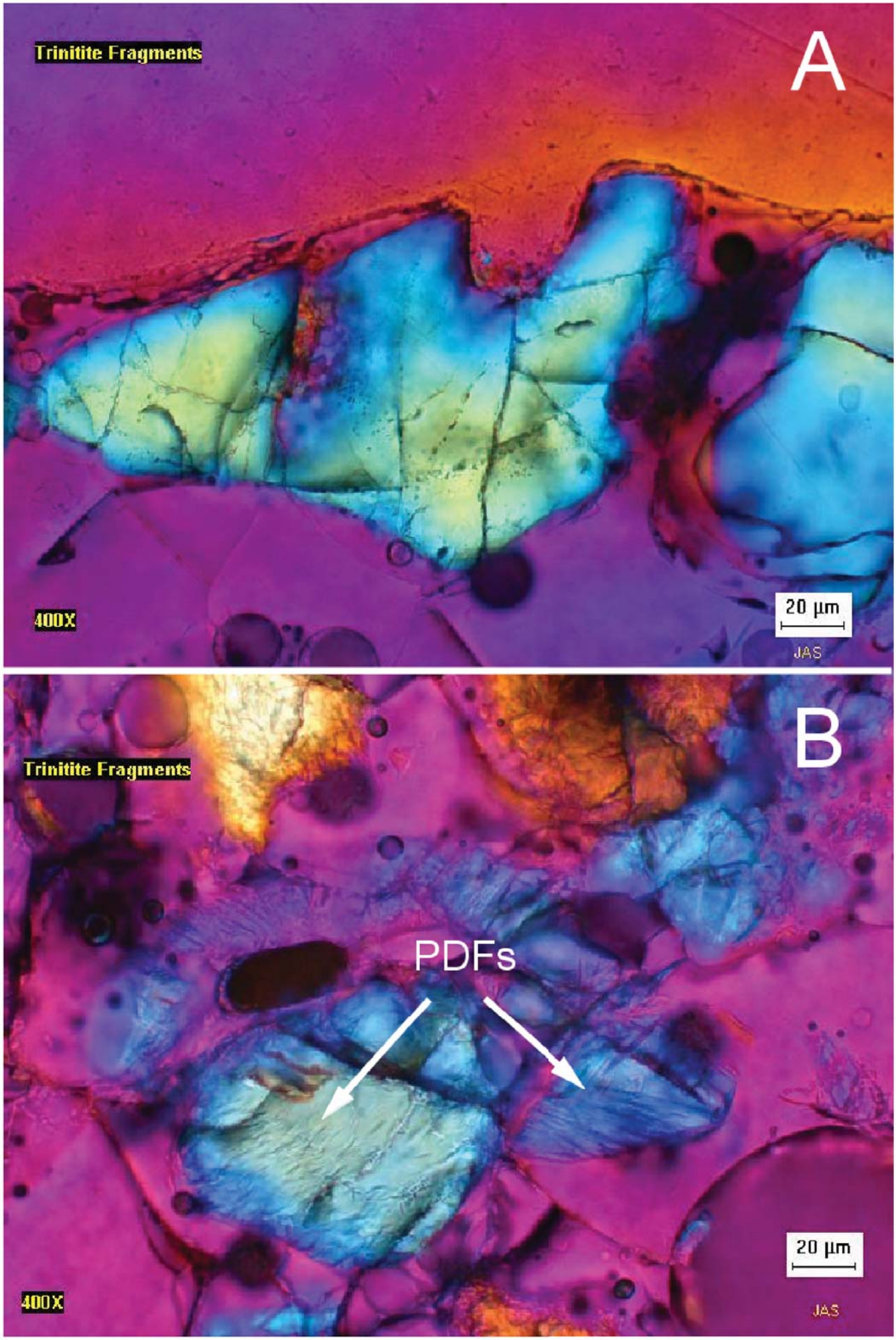
Trinitite Fragments
A
400X
20 µm
JAS
Trinitite Fragments
B
PDFs
400X
20 µm
JAS

Figure 10

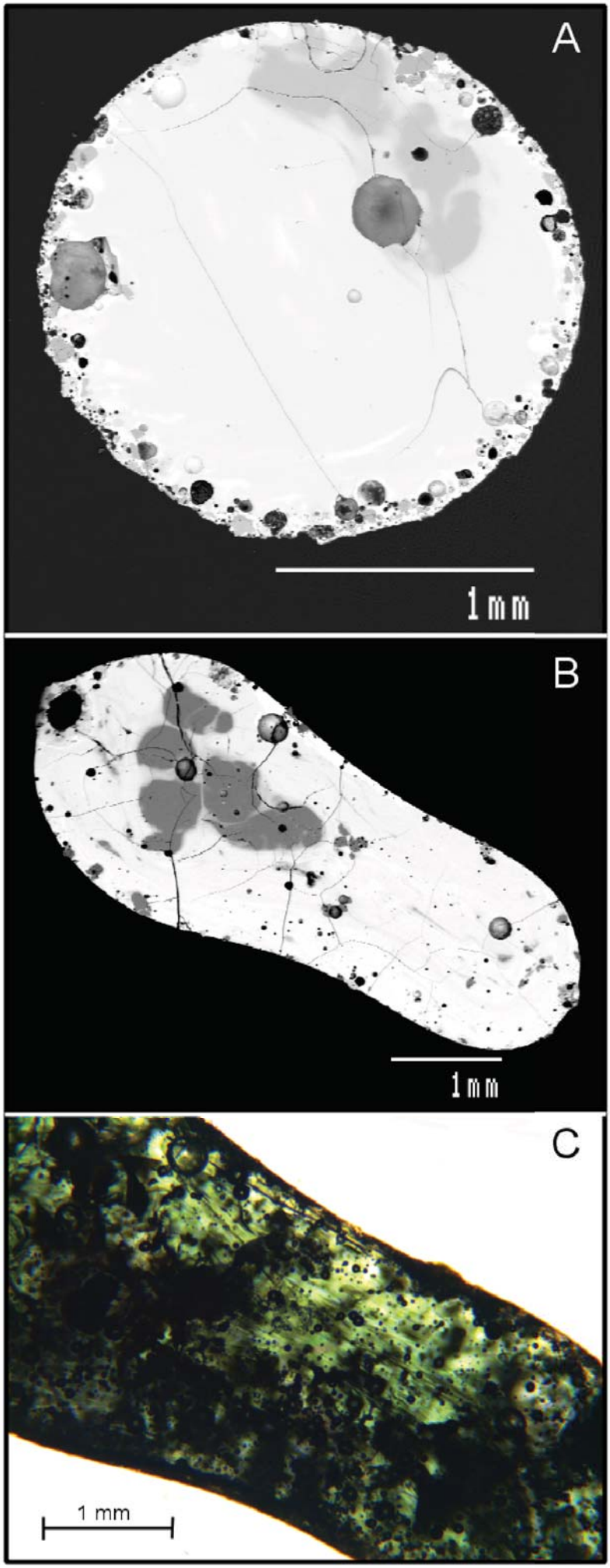

Figure 11

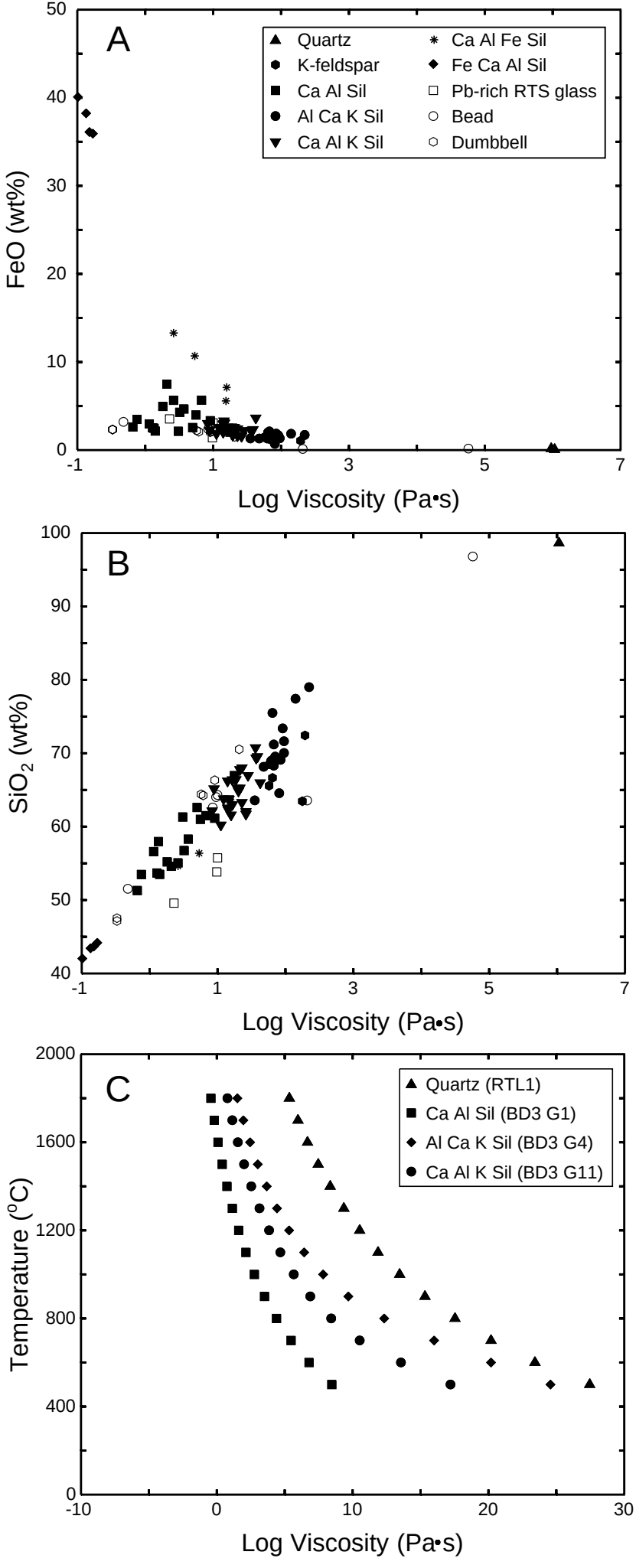
A
Quartz
K-feldspar
Ca Al Sil
Al Ca K Sil
Ca Al K Sil
Ca Al Fe Sil
Fe Ca Al Sil
Pb-rich RTS glass
Bead
Dumbbell
FeO (wt%)
Log Viscosity (Pa•s)
B
SiO2 (wt%)
Log Viscosity (Pa•s)
C
Quartz (RTL1)
Ca Al Sil (BD3 G1)
Al Ca K Sil (BD3 G4)
Ca Al K Sil (BD3 G11)
Temperature (°C)
Log Viscosity (Pa•s)

Figure 12

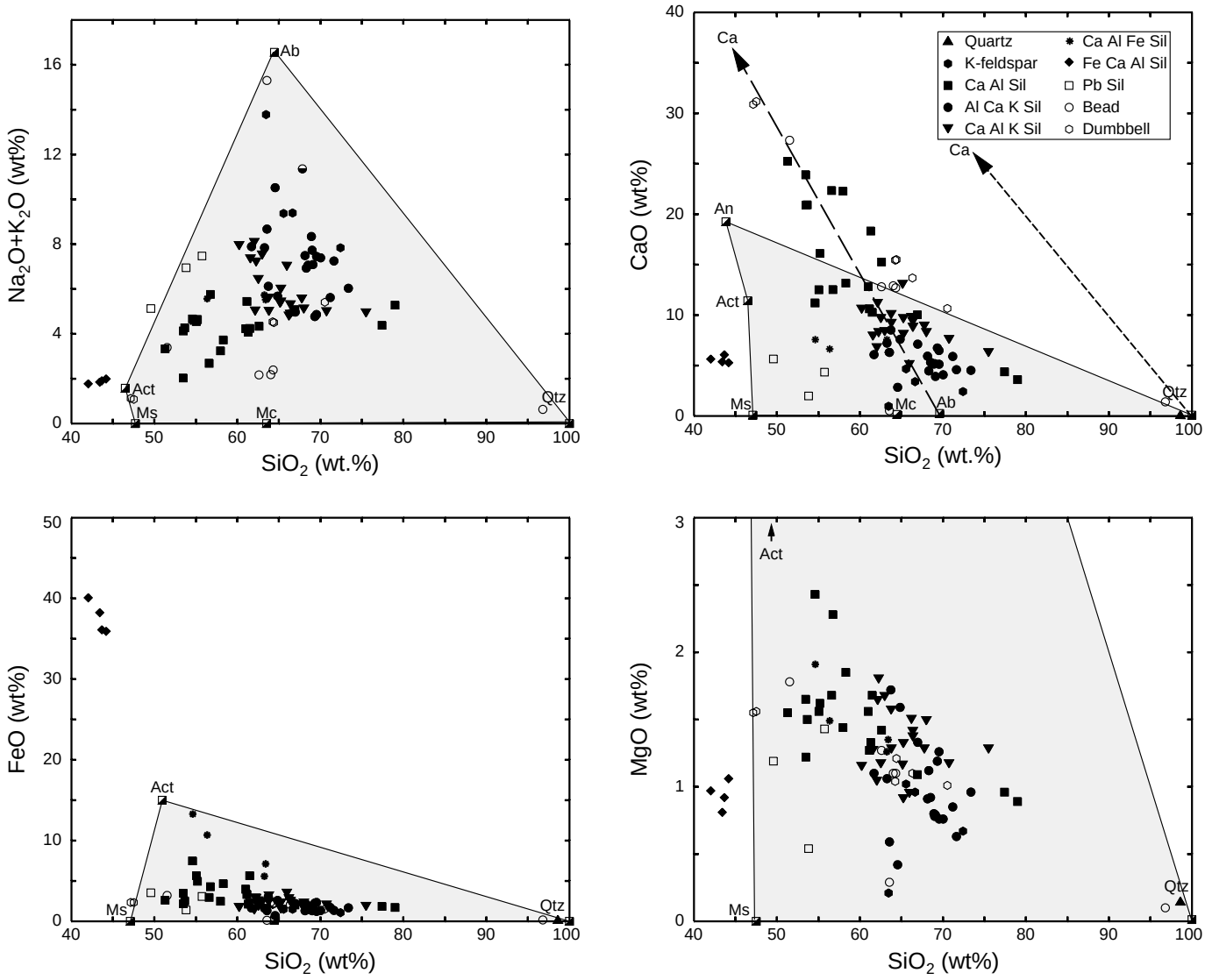
Na2O+K2O (wt%)
SiO2 (wt.%)
Ab
Act
Ms
Mc
Qtz
CaO (wt%)
SiO2 (wt.%)
Ca
An
Act
Ms
Mc
Ab
Qtz
Quartz
K-feldspar
Ca Al Sil
Al Ca K Sil
Ca Al K Sil
Ca Al Fe Sil
Fe Ca Al Sil
Pb Sil
Bead
Dumbbell
FeO (wt%)
SiO2 (wt%)
Act
Ms
Qtz
MgO (wt%)
SiO2 (wt%)
Act
Ms
Qtz

Figure 13

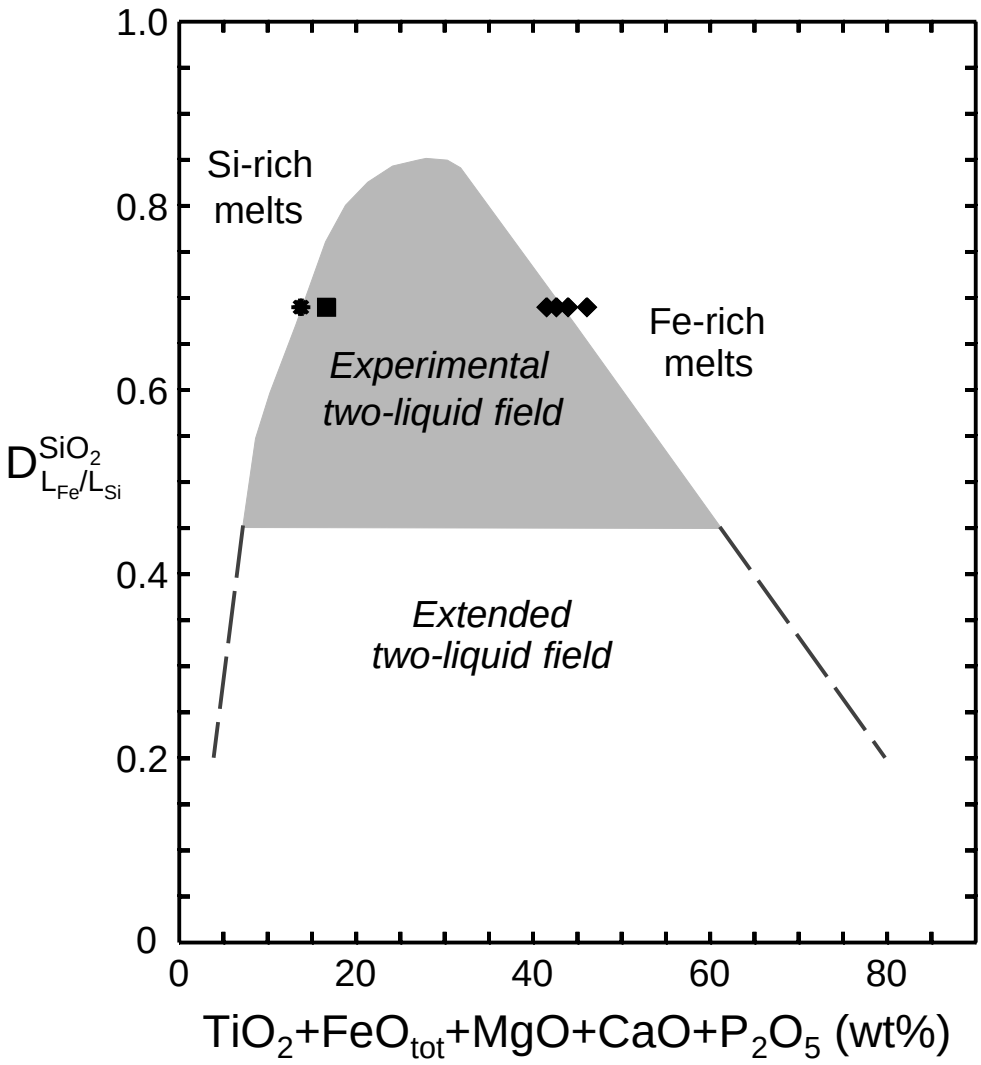
1.0
0.8
0.6
0.4
0.2
0
0
20
40
60
80
Si-rich
melts
Fe-rich
melts
Experimental
two-liquid field
Extended
two-liquid field
$D^{SiO_2}_{L_{Fe}/L_{Si}}$
$TiO_2+FeO_{tot}+MgO+CaO+P_2O_5$ (wt%)

Figure 14